Chapter 2
High-Frequency Sound Generated by Sound-Aerofoil Interaction in Subsonic Uniform Flow

In this chapter we adapt the analytically-based procedure of (Myers and Kerschen 1995, 1997) and Tsai (1992) to study the sound-aerofoil interaction problem. We consider a high-frequency incident plane sound wave being scattered by a generic aerofoil (such as that in Fig. 1.7) in a steady uniform background flow, and use the asymptotic limits as described in the Introduction; $k \gg 1$ is the acoustic reduced frequency; $\epsilon \ll 1$ is a non-dimensionalised small parameter (lengths are non-dimensionalised with respect to semi-chord length) such that $t = \epsilon t'$ and $\alpha = \epsilon \alpha'$ are the thickness and camber, respectively, of the aerofoil; and we impose that $\epsilon k = O(1)$. Results will be shown specifically for NACA 4-digit series aerofoils, however any aerofoil with a parabolic nose is allowable. In Sect. 2.2 we discuss this nose shape constraint and allude to results for bodies with different nose shapes, and later in Chap. 4 we explicitly discuss elliptic-nosed bodies (although in both of these cases the radius of curvature of the nose is $O(\epsilon^2)$). The method of matched asymptotic expansions, (Van Dyke 1975), is used to split the problem into several asymptotic regions around the aerofoil; the inner leading- and trailing-edge regions, of size $O(k^{-1})$ centred on the leading and trailing edges respectively; the transition regions on the aerofoil surfaces between the inner leading- and trailing-edge regions, of width $O(k^{-1/2})$, which account for the surface curvature of the aerofoil; a wake region, also of width $O(k^{-1/2})$; and the outer region comprising the rest of space, which also contains Fresnel zones above and below the aerofoil emanating from the leading and trailing edges. The solution in each region is determined individually, and matched to its surrounding regions using Van Dyke's matching rule (Van Dyke 1975). An advantage of this analytical approach is that it provides results in the high-frequency regime (where numerical approaches become more difficult) as well as providing interesting physical insight.

In Sect. 2.1 we formulate the mathematical problem for the incidence of a high-frequency sound wave on an aerofoil. In Sect. 2.2 we solve the governing equations in the inner leading-edge region of the aerofoil. On taking the outer limit of this inner solution (as required by the matching process) we find singularities along the

© Springer International Publishing Switzerland 2015

L. Ayton, *Asymptotic Approximations for the Sound Generated by Aerofoils in Unsteady Subsonic Flows*, Springer Theses,
DOI 10.1007/978-3-319-19959-7_2

shadow and reflection boundaries, so we construct uniformly-valid expansions to eliminate these singularities in the far-field solution. The leading-order solution (the flat-plate solution) yields the well-known uniformly-valid expansion containing the complementary error function, and is caused by the coalescence of a saddle point and a pole in a very familiar way (Jones 1986). In contrast, the part of the leading-order thickness correction which accounts for the inclination of the surface normal vector has a singularity caused by the coalescence of a branch cut and a saddle point, and the uniformly-valid solution is more unusual, containing a modified Bessel function of the second kind. In Sect. 2.3 we construct the leading-edge outer, and surface transition solutions, the latter of which accounts for the surface curvature of the aerofoil. In Sect. 2.4 we find the trailing-edge outer, transition and inner solutions; the inner solution comprises of the field arising from the scattering of the leading-edge field by the trailing edge, which is similar to that found in Myers and Kerschen (1997) and Tsai (1992), and the reflected field, which is particular to our incident sound problem. This reflected field generates further Fresnel regions, now emanating from the trailing edge, which have the standard far-field form involving the complementary error function. The final uniformly-valid result of the total far-field sound generated when a sound wave is scattered and reflected by a thin aerofoil in background steady uniform flow is presented in Sect. 2.5. Section 2.6 contains results and discussion, and concluding remarks are given in Sect. 2.7.

2.1 Formulation of the Problem

2.1.1 Aerofoil Geometry and Steady Mean Flow

We consider a small unsteady perturbation to the mean flow around a thin aerofoil of chord length $2b^*$ in Cartesian coordinates (x^*, y^*) with their origin at the aerofoil leading edge. We use * to denote dimensional quantities. We restrict the geometry of the aerofoil to have a parabolic nose $(\epsilon y^*(x^*) \sim 2a\epsilon t'\sqrt{x^*/b^*}$ at the leading edge, where $t = \epsilon t'$ is the maximum thickness of the aerofoil as a fraction of the chord length and primed quantities are $O(1))$ and a sharp trailing edge. We decompose the boundary description of the aerofoil, $\epsilon y^*(x^*)$, into thickness related terms, $\epsilon y^{(t)*}$, and camber and angle of attack related terms, $\epsilon Y^{(c)*}(x^*) = -\alpha_i x^* + \epsilon y^{(c)*}(x^*)$, where α_i is the angle of attack, and $y^{(c)}$ describes the camber line of the aerofoil.

In what follows we non-dimensionalise lengths with respect to b^*, and velocities by U^*_∞, where U^*_∞ is the uniform mean flow speed far from the aerofoil. Note this non-dimensionalisation fails when there is no background mean flow, but we do not consider such a simplified case. At upstream infinity the mean flow is uniform, with speed U^*_∞ aligned with the positive x^* direction. It is most convenient to work in the non-dimensionalised orthogonal coordinate system (ϕ, ψ), which represent the

velocity potential and streamfunction of the mean flow around the aerofoil. In this coordinate system we write $z = \phi + \mathrm{i}\psi$, which relates to the Cartesian coordinates (x, y) via

$$x + \mathrm{i}\beta_\infty y = z + O(\epsilon), \tag{2.1.1.1}$$

where $\beta_\infty^2 = (1 - M_\infty^2)$ is the Prandtl-Glauert transformation factor accounting for compressibility, and M_∞ is the mean flow Mach number at upstream infinity.

To utilise the modified rapid distortion theory equations determined by Kerschen and Myers (1987), we need the complex potential for the steady flow around the aerofoil. Using Thwaites (1960) we find that, for a thin aerofoil, the amplitude of the total mean flow is $U_\infty^*(1 + \epsilon q)$, in the direction making an angle $\epsilon\mu$ with the x^* axis, where

$$(q - \mathrm{i}\mu)(z) = \frac{1}{\pi\beta_\infty}\int_0^2 \frac{y^{(t)\prime}(x)}{z - x}dx + \frac{1}{\pi\beta_\infty}\sqrt{\frac{2 - z}{z}}\int_0^2 \frac{Y^{(c)\prime}(x)}{z - x}\sqrt{\frac{x}{2 - x}}dx, \tag{2.1.1.2}$$

and $'$ denotes differentiation. This is correct to first order in aerofoil thickness, camber and angle of attack. The quantities q and μ are related to the complex potential F (which is non-dimensionalised with respect to $U_\infty^{*2}b^*$) by

$$q(\phi, \psi) - \mathrm{i}\mu(\phi, \psi) = \frac{dF}{dz}, \tag{2.1.1.3}$$

where the arbitrary constant in F is chosen so that $F(0) = 0$. This now completes the relation given by (2.1.1.1); the $O(\epsilon)$ perturbation is $\epsilon F(z)$. We require explicit details of q and μ in the local neighbourhood of the leading and trailing edges. For the other regions we construct the unsteady solution in terms of q, μ, and F. For further details of the coordinate transformation between physical (x, y)-space, and potential-streamline space, see Myers (1987).

We combine the angle of attack, $\alpha_i = \epsilon\alpha_i'$, and the leading-edge camber together to give an effective angle of attack, $\alpha_{\text{eff}} = \epsilon\alpha_{\text{eff}}'$, with

$$\alpha_{\text{eff}} = \alpha_i - \frac{1}{\pi}\int_0^2 \frac{\epsilon y^{(c)}(x)(1 - x)}{((2 - x)x)^{3/2}}dx. \tag{2.1.1.4}$$

Equation (2.1.1.4) has been found by sending $z \to 0$ in the second term in (2.1.1.2) and integrating by parts so that later, with this effective angle of attack, we may write the inner leading-edge expansion of q as $q - \mathrm{i}\mu \sim \alpha_{\text{eff}}'\beta_\infty^{-1}\sqrt{2}z^{-1/2} +$ thickness term $+ O(z^{1/2})$. The complex velocity potential for a general thin aerofoil with boundary $\epsilon y(x) = \epsilon y^{(t)}(x) + \epsilon y^{(c)}(x)$, where t and c denote thickness and camber respectively, can be written as $F = F_0 + F^{(t)} + F^{(c)}$, where F_0 is the flat-plate

potential at angle of attack α_i as given in Myers and Kerschen (1995). The flat-plate (at the angle of attack), thickness and camber dependent components of the complex potential are given by

$$F_0(z) = \frac{\mathrm{i}\alpha_i}{\beta_\infty}\left(\log\left[z-1+\sqrt{z(z-2)}\right]+z-\sqrt{z(z-2)}-\pi\mathrm{i}\right), \tag{2.1.1.5}$$

$$F^{(c)}(z) = \frac{-\mathrm{i}}{\pi\beta_\infty}\int_0^2 y^{(c)\prime}(x)\frac{\sqrt{x}}{\sqrt{2-x}}\left(\log\left[\frac{1+\sqrt{(z-2)/z}}{1-\sqrt{(z-2)/z}}\right]\right.$$
$$\left.-\,\mathrm{i}\frac{\sqrt{2-x}}{\sqrt{x}}\log\left[\frac{\mathrm{i}\sqrt{(2-x)/x}+\sqrt{(z-2)/z}}{\mathrm{i}\sqrt{(2-x)/x}-\sqrt{(z-2)/z}}\right]-\pi\mathrm{i}\right)dx, \tag{2.1.1.6}$$

$$F^{(t)}(z) = \frac{1}{\pi\beta_\infty}\left(\int_0^2 y^{(t)\prime}(x)\log[z-x]dx+\int_0^2\frac{y^{(t)\prime}(x)}{x}dx\right). \tag{2.1.1.7}$$

This completes our description of the mean flow.

A shift of $z \to z+2$ recentres the expressions for the disturbance potentials about the trailing edge (where now we take constants such that the velocity potential with respect to trailing-edge coordinates, F_t, satisfies $F_t(z_t = 0) = 0$). These are used later to determine the phase shift between the leading- and trailing-edge scattered fields.

2.1.2 Unsteady Disturbance Equations

Rapid distortion theory is often used to investigate the sound generated by the interaction of an unsteady flow with a solid boundary. The theory was initially developed by Hunt (1973) and Goldstein (1978) for three-dimensional incompressible and compressible flows respectively, but the form given by Kerschen and Myers (1987) and Kerschen and Balsa (1981) for two-dimensional, small-disturbance mean flows is more relevant to this chapter. We assume that the fluid is inviscid and non heat conducting, which is a reasonable assumption in many aeronautical applications such as fan noise. For the purposes here we assume that the incident sound wave originates far from the aerofoil where the mean flow is uniform, with a small-amplitude unsteady disturbance. The third coordinate in our orthogonal system (ϕ^*, ψ^*, x_3^*) is the spanwise direction, and we assume that all unsteady quantities are proportional to $\mathrm{e}^{ik_3x_3-i\omega t}$, where ω is the non-dimensionalised frequency. We non-dimensionalise coordinates (ϕ^*, ψ^*) with respect to $U_\infty^* b^*$, wavevector $\boldsymbol{k} = k^*(k_1, k_2, k_3)$ with respect to $(b^* U_\infty^*)^{-1}$ and frequency with respect to $k^* U_\infty^{*2}$.

We assume the perturbation to the uniform flow, due to the presence of the aerofoil, is small compared to the uniform flow component, but large compared to the unsteady flow component. Following Kerschen and Myers (1987) we use the perfect gas relations for a small velocity perturbation, ϵq, to a uniform mean flow and take directly from them the governing equation for the modified unsteady velocity

potential $h(\phi, \psi)$ (Kerschen and Myers 1987, Eq. 10). Here h relates to the physical unsteady velocity potential, G, via

$$h(\phi, \psi) = G(\phi, \psi)\mathrm{e}^{-\mathrm{i}k_3 x_3 + \mathrm{i}\omega t}\mathrm{e}^{\mathrm{i}kM_\infty^2\phi/\beta_\infty - M_\infty^2 \epsilon q}, \tag{2.1.2.1}$$

and G satisfies

$$\frac{D_0}{Dt}\left(\frac{1}{a_0}\frac{D_0 G}{Dt}\right) - \frac{1}{\rho_0}\nabla\cdot(\rho_0 \nabla G) = \frac{1}{\rho_0}\nabla\cdot(\rho_0 v)\,, \tag{2.1.2.2}$$

where the perturbation to the steady mean flow field is given by $\boldsymbol{u} = \boldsymbol{v} + \nabla G$ and $\boldsymbol{v}$ is the evolution of the incident vortical disturbance in the steady mean flow. In Goldstein (1978), the flow field is separated into $\boldsymbol{v}$ and G because (in the case of an incident gust) one, G, can then be seen as an acoustic field, and the other, $\boldsymbol{v}$, a vortical field. In this chapter, we are considering the effects of an acoustic incident field only, therefore we set $\boldsymbol{v} = \boldsymbol{0}$, and we separate G into two parts, one that is the imposed perturbation, and one that is the response. Individually both fields satisfy (2.1.2.2) with zero source term. We solve (2.1.2.2) for the imposed incident field in the next subsection, whilst the remainder of the chapter focuses on solving for the response by imposing a boundary condition on the aerofoil surface. The incident sound field is denoted by a subscript $_I$ whilst the response has no subscript.

The subscript $_0$ denotes steady mean flow quantities, and ρ_0 and a_0 are density and speed of sound respectively. We can determine the mean flow quantities with respect to their values far upstream (denoted by subscript $_\infty$), via

$$\frac{U_0}{U_\infty} = 1 + \epsilon q, \qquad \frac{V_0}{V_\infty} = \epsilon\mu, \tag{2.1.2.3a}$$

$$\frac{a_0}{a_\infty} = 1 - \epsilon\frac{\gamma-1}{2}M_\infty^2 q, \qquad \frac{\rho_0}{\rho_\infty} = 1 - \epsilon M_\infty^2 q, \tag{2.1.2.3b}$$

$$\frac{\beta_0}{\beta_\infty} = 1 - \epsilon\left(1 + \frac{\gamma-1}{2}M_\infty^2\right)\frac{M_\infty^2}{\beta_\infty^2}q, \qquad \frac{M_0}{M_\infty} = 1 + \epsilon\left(1 + \frac{\gamma-1}{2}M_\infty^2\right)q. \tag{2.1.2.3c}$$

These expansions are correct to first order in ϵ, and γ is the ratio of specific heats.

After non-dimensionalisation of (2.1.2.2), we retain terms of size $O(k^2, k, 1)$ (recall $k = O(\epsilon^{-1})$), to find the governing equation for h,

$$\frac{\partial^2 h}{\partial\phi^2} + \frac{\partial^2 h}{\partial\psi^2} + k^2 w^2(1 - 2\beta_\infty^2\epsilon q)h + \frac{(\gamma+1)M_\infty^4\epsilon q}{\beta_\infty^2}\left(\frac{\partial^2 h}{\partial\psi^2} + 2\mathrm{i}k\delta\frac{\partial h}{\partial\phi} + k^2(w^2+\delta^2)h\right) - \frac{(\gamma+1)M_\infty^4}{\beta_\infty^2}\epsilon\frac{\partial q}{\partial\phi}\left(\frac{\partial h}{\partial\phi} - \mathrm{i}k\delta h\right) = 0, \tag{2.1.2.4a}$$

where

$$\delta = \frac{\omega}{\beta_\infty^2}, \qquad w^2 = (\delta M_\infty)^2 - (k_3/\beta_\infty)^2. \tag{2.1.2.4b}$$

In (2.1.2.4) we have now explicitly set the source term from (2.1.2.2) to zero.

We work with the modified unsteady pressure, as defined by Myers and Kerschen (1995, Eq. (2.7)), which is given by

$$p = -\left(\frac{\partial h}{\partial \phi} - \mathrm{i}k\delta h\right) \mathrm{e}^{-\mathrm{i}k\delta M_\infty^2 \phi}. \tag{2.1.2.5}$$

In the following sections we solve for h in various regions around the aerofoil, wherein different terms dominate the behaviour of the flow. These regions arise from balancing different terms in (2.1.2.4) with respect to k and ϵ. We have a particular aim of finding the acoustic pressure in the far field.

2.1.3 Form of the Incident Sound

Suppose the incident sound wave has potential

$$h_I = A_I \mathrm{e}^{\mathrm{i}kw\sigma_I}. \tag{2.1.3.1}$$

We require $A_I = 1$, and $\sigma_I = k_1\phi + k_2\psi$ at infinity, where $k_{1,2}$ are the streamwise and transverse wavenumbers of the incident sound wave. Writing $\sigma_I = \sigma_0 + \epsilon\sigma_1 + O(\epsilon^2)$ and substituting (2.1.3.1) into (2.1.2.4) we find that to $O(k^2)$

$$\left(\frac{\partial \sigma_0}{\partial \phi}\right)^2 + \left(\frac{\partial \sigma_0}{\partial \psi}\right)^2 - 1 = 0. \tag{2.1.3.2}$$

Hence $\sigma_0 = k_1\phi + k_2\psi$ subject to $k_1^2 + k_2^2 = 1$. We define χ as the angle of propagation of the sound wave with respect to the uniform flow upstream, and write $(k_1, k_2) = (\cos\chi, \sin\chi)$. The sound originates from upstream, $-\pi/2 < \chi < \pi/2$, or from downstream $\pi/2 < \chi < 3\pi/2$. The real part of (2.1.2.4) to $O(k)$ gives the eikonal equation

$$\cos\chi \frac{\partial \sigma_1}{\partial \phi} + \sin\chi \frac{\partial \sigma_1}{\partial \psi} + q\left(\beta_\infty^2 - \frac{(\gamma+1)M_\infty^4}{2\beta_\infty^2 w^2}(\delta - w\cos\chi)^2\right) = 0, \tag{2.1.3.3}$$

whilst the imaginary part at this order gives the transport equation

$$\frac{\partial A_I}{\partial \phi}\cos\chi + \frac{\partial A_I}{\partial \psi}\sin\chi = 0. \tag{2.1.3.4}$$

By using characteristic coordinates $\xi = \phi + \psi\cot\chi, \eta = \phi - \psi\cot\chi$ and re-labelling $q(\phi,\psi)$ as $\mathcal{Q}(\xi,\eta)$ in these variables, we obtain the solution to the eikonal equation

$$\sigma_1 = \frac{V(\chi)}{2\cos\chi}\int_{-\infty}^{\xi}\mathcal{Q}(\xi',\eta)d\xi', \tag{2.1.3.5}$$

where

$$V(\theta) = -\beta_\infty^2\left(1 - \frac{(\gamma+1)M_\infty^4}{2\beta_\infty^4 w^2}(\delta - w\cos\theta)^2\right). \tag{2.1.3.6}$$

The function σ_1 represents the distortion of the incident sound wave due to the non-uniform steady flow created by the presence of the aerofoil. We set g_1 to zero due to the condition at infinity. The transport equation is satisfied by an arbitrary function of the spanwise coordinate, x_3, but given the condition at infinity we set $A_I = 1$ everywhere, and hence the incident sound wave is given by

$$h_I = \exp\left(\mathrm{i}kw(\phi\cos\chi + \psi\sin\chi) + \frac{\mathrm{i}k\epsilon w V(\chi)}{2\cos\chi}\int_{-\infty}^{\xi}\mathcal{Q}(\xi',\eta)d\xi'\right). \tag{2.1.3.7}$$

If $\chi = \pi/2$, we can solve for σ_1 directly from (2.1.3.3) without changing to characteristic variables. This special case shall not be considered further. The boundary condition for the problem is one of zero unsteady normal velocity on the aerofoil surface, i.e.

$$\left(\frac{\partial h}{\partial\psi} + M_\infty^2\epsilon\frac{\partial q}{\partial\psi}h\right)_{\psi=0} = -\left(\frac{\partial h_I}{\partial\psi} + M_\infty^2\epsilon\frac{\partial q}{\partial\psi}h_I\right)_{\psi=0}. \tag{2.1.3.8}$$

Here $\psi = 0$ corresponds to the aerofoil surface and the range of ϕ over which (2.1.3.8) holds corresponds to the body length in the (ϕ,ψ) plane.

We use the method of matched asymptotic expansions (Van Dyke 1975) to solve the problem in all regions shown in Fig. 2.1; solving (i) and (ii) in Sect. 2.2, specifically with (ii) occurring in Sects. 2.2.1–2.2.5; solving (iii) in Sects. 2.3.1 and 2.4.1; solving (iv) in Sect. 2.3.2; solving (v) and (vi) in Sect. 2.4.2; and finally solving (vii) in Sect. 2.4.3. As in Myers and Kerschen (1997), we take $k \gg 1$ and $\epsilon \ll 1$ with the distinguished limit that $\epsilon k = O(1)$, but with suitable choice of $O(1)$ parameters t' and α' (recall thickness and camber angle of the aerofoil are measured by, $t = \epsilon t'$ and $\alpha = \epsilon\alpha'$), our analysis also holds for flat-plate or uncambered aerofoils. We begin with the leading-edge inner region, then match that to the leading-edge outer region. The leading-edge transition region along the aerofoil surface can then be constructed. A similar process is completed at the trailing edge, but to ensure continuity of pressure at the trailing edge, these solutions rely on the leading-edge solution, and thus are more complicated.

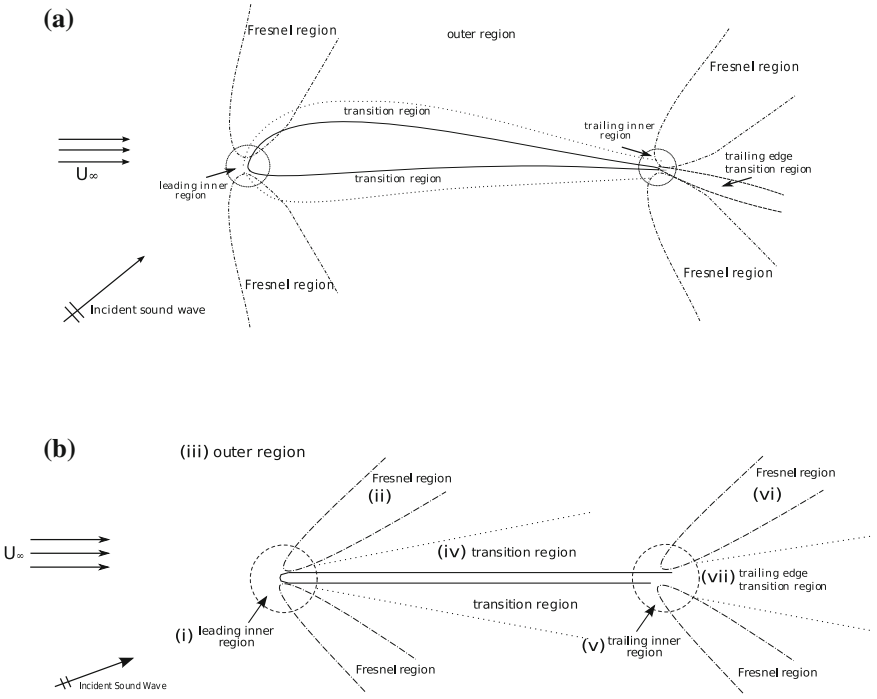

Fig. 2.1 Asymptotic regions around the aerofoil; leading—and trailing-edge inner regions, (*i*) and (*v*), scale as $O(k^{-1})$, the width of the transition regions, (*iv*) and (*vii*), scales as $O(k^{-1/2})$, and the width of the Fresnel regions, (*ii*) and (*vi*), scales as $O((kr)^{1/2})$. The outer region (*iii*) is $O(1)$ on the scale of the aerofoil chord. We solve for (*i*) in Sect. 2.2, with (*ii*) found specifically in Sects. 2.2.1–2.2.5. We then solve for a leading-edge contribution to (*iii*) in Sect. 2.3.1, and (*iv*) in Sect. 2.3.2. We solve for the trailing-edge contribution to (*iii*) in Sect. 2.4.1, solve for (*v*) and (*vi*) in Sect. 2.4.2, and finally for (*vii*) in Sect. 2.4.3. **a** In (x, y) space. **b** In (ϕ, ψ) space

2.2 Leading-Edge Inner Solution

Here we introduce inner variables $(\Phi, \Psi) = k(\phi, \psi)$ for $k \gg 1$ centred on the leading edge, and require the inner expansion of (2.1.1.2). To obtain this, we take the approximation of the aerofoil boundary near the leading edge in inner variables, substitute into (2.1.1.2), and expand for large k. Recalling that $y^{(t)} \sim 2a\epsilon t'\sqrt{x}$ as $x \to 0$, and α_{eff} is defined in (2.1.1.4) as a function of the angle of attack and the camber distribution, the result is

$$(q - \mathrm{i}\mu)(R, \theta) \sim -\frac{at'\mathrm{i}}{\beta_\infty}\sqrt{\frac{k}{R}}(\cos\theta/2 - \mathrm{i}\sin\theta/2) + \frac{\alpha'_{\text{eff}}}{\beta_\infty}\sqrt{\frac{2k}{R}}(\cos\theta/2 - \mathrm{i}\sin\theta/2), \tag{2.2.0.1}$$

where (R, θ) are the local polar coordinates centred on $(0, 0)$ with $R = kr$. Transforming the Eqs. (2.1.2.4) gives

$$\frac{\partial^2 H}{\partial \Phi^2}+\frac{\partial^2 H}{\partial \Psi^2}+w^2(1-2\beta_\infty^2\epsilon q)H+\frac{(\gamma+1)M_\infty^4}{\beta_\infty^2}\epsilon q\left(\frac{\partial^2 H}{\partial \Psi^2}+2\mathrm{i}\delta\frac{\partial H}{\partial \Phi}+(w^2+\delta^2)H\right)$$
$$-\frac{(\gamma+1)M_\infty^4}{\beta_\infty^2}\epsilon\frac{\partial q}{\partial \Phi}\left(\frac{\partial H}{\partial \Phi}-\mathrm{i}\delta H\right)=0, \qquad (2.2.0.2a)$$

subject to the boundary condition of zero normal velocity on the aerofoil surfaces, $\psi = 0$, i.e.

$$\frac{\partial H}{\partial \Psi}+M_\infty^2\epsilon\frac{\partial q}{\partial \Psi}H\bigg|_{\Psi=0\pm}=-\left[\frac{1}{k}\frac{\partial h_I}{\partial \psi}+M_\infty^2\epsilon\frac{\partial q}{\partial \Psi}h_I\right]_{\Psi=0\pm}, \qquad (2.2.0.2b)$$

where H is the unsteady potential in the inner region. This boundary condition tells us that $H = O(1)$ at leading order. We now follow Myers and Kerschen (1997) and Tsai (1992), and expand the inner unsteady potential in the form;

$$H(\Phi,\Psi)=\mathrm{e}^{\mathrm{i}kw\sigma_1(0,0)}\left(H_0+\epsilon t'\sqrt{k}(H_1+H_2+H_3)+\epsilon\alpha'_{\mathrm{eff}}\sqrt{k}(P_1+P_2+P_3)+O(\epsilon)\right). \qquad (2.2.0.3)$$

Here, the phase function, σ_1, is given by (2.1.3.5) and arises due to the distortion of the incident sound wave through the non-uniform flow at the nose. Of the remaining functions, H_0 is the flat plate solution at zero angle of attack, $H_{1,2,3}$ are thickness-dependent terms, and $P_{1,2,3}$ are camber and angle of attack dependent terms. In what follows we determine each of these terms.

We mention here the requirement to have a parabolic-nosed body, $y \sim 2a\epsilon t'\sqrt{x}$. We choose this shape so that we may analyse the inner region qualitatively, and in particular obtain (2.2.0.1) and (2.2.0.3). For an arbitrary nose, $y \sim \epsilon t' x^m$, where $0 < m < 1$ we would obtain $q \sim (k/R)^{m-1}$ thus the asymptotic series, (2.2.0.3), would be $H_0 + \epsilon k^m \mathcal{H}_1$. We would proceed to match orders of ϵk^m in the governing equation and boundary conditions as illustrated in the coming sections, but would have an additional arbitrary quantity, m. The parabolic nose choice, $m = 1/2$, conforms to the NACA 4-digit series of aerofoil that are commonplace in the literature of blade-blade interaction problems, hence we impose this from the beginning to ease the understanding of the analysis.

2.2.1 Solution for the Flat-Plate Term H_0

The leading-order solution is simply that found for a semi-infinite flat plate at zero angle of attack with an incident sound wave in uniform flow. It satisfies

$$D(H_0)=0, \qquad (2.2.1.1a)$$

$$\frac{\partial H_0}{\partial \Psi}\bigg|_{\substack{\Phi>0\\ \Psi=0}}=-\mathrm{i}w\sin\chi\,\mathrm{e}^{\mathrm{i}w\cos(\chi)\Phi}, \qquad (2.2.1.1b)$$

where

$$D = \frac{\partial^2}{\partial \Phi^2} + \frac{\partial^2}{\partial \Psi^2} + w^2. \tag{2.2.1.2}$$

This is of the same form as the flat-plate problem for an incident gust, and only depends on the aerofoil surface blocking the normal component of the incident velocity. Using the Wiener-Hopf technique in a standard way (see Myers and Kerschen 1995 for more details), we obtain the solution

$$H_0 = -\frac{\mathrm{i}\sqrt{w}\sin(\chi)\mathrm{sgn}(\Psi)}{2\pi\sqrt{\cos\chi + 1}} \int_{-\infty}^{\infty} \frac{\mathrm{e}^{-\mathrm{i}\lambda\Phi - |\Psi|\sqrt{\lambda^2 - w^2}}}{(\lambda + w\cos\chi)\sqrt{\lambda + w}} d\lambda. \tag{2.2.1.3}$$

Expanding (2.2.1.3) for large R, for later matching to the outer solution, gives

$$H_0 \sim L_0(\theta)\frac{\mathrm{e}^{\mathrm{i}kwr}}{\sqrt{kr}} + H_0^p + O(k^{-3/2}), \tag{2.2.1.4a}$$

$$L_0(\theta) = -\frac{\mathrm{i}\sin\chi \mathrm{e}^{-\mathrm{i}\pi/4}\cos\theta/2}{\sqrt{\pi}\sqrt{w\cos\chi + w}(\cos\chi - \cos\theta)}. \tag{2.2.1.4b}$$

H_0^p is the contribution from the pole at $\lambda = -w\cos\chi$, which may or may not be included, depending on where the pole lies in relation to the steepest descent contour for the function

$$a(\lambda) = -\mathrm{i}\lambda R\cos\theta - R|\sin\theta|\sqrt{\lambda^2 - w^2}. \tag{2.2.1.4c}$$

See Fig. 2.2 for an illustration of the steepest descent contour. In fact,

$$H_0^p = -\mathrm{sgn}(\Psi)\mathrm{e}^{\mathrm{i}w\cos(\chi)\Phi + \mathrm{i}w\sin(\chi)|\Psi|} \tag{2.2.1.5}$$

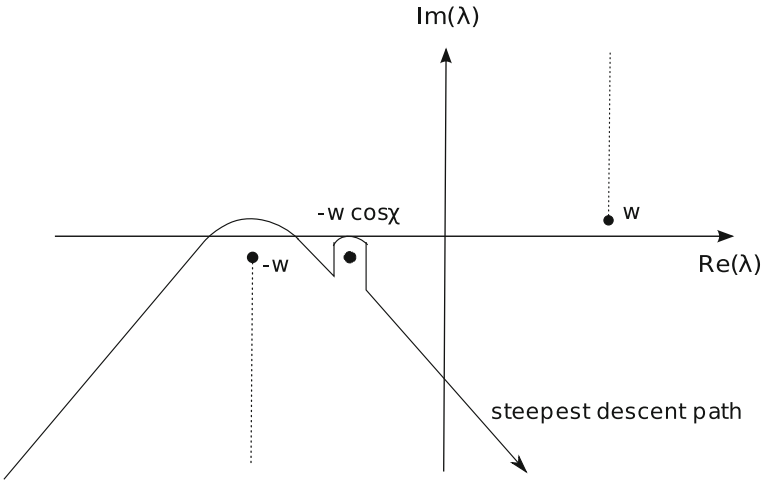

Fig. 2.2 Steepest descents contour for phase function $-a(\lambda)$ in the λ-plane

if $0 < \theta < \chi$ or $2\pi - \chi < \theta < 2\pi$, and H_0^p is zero otherwise. This pole represents shadow, $0 < \theta < \chi$, and reflection, $2\pi - \chi < \theta < 2\pi$, regions of the incident sound wave by a semi-infinite flat plate. There is no pole in the gust case of Myers and Kerschen (1997), therefore for them, L_0 would be uniformly valid, however for the sound-aerofoil case, our expression for L_0 has two regions of non-uniformity, i.e. when $\cos\chi = \cos\theta$, which is caused in a very familiar way by the coincidence of the pole in the integrand of (2.2.1.3) and the saddle point arising in the determination of the outer limit.

The uniformly-valid outer limit of (2.2.1.3) can be found using standard methods (Jones 1986) which we outline here; upon deforming the contour to the steepest descents contour (see Fig. 2.2) we cross the pole and pick up the contribution from H_0^p which, for $\Phi > 0$ is the reflection of the incident wave, and for $\Phi < 0$ is a cancellation of the incident wave, i.e. a shadow region. The regions determined by the reflection/shadow are bounded by angles which generate the discontinuity in the standard geometric optic far-field solution, (2.2.1.4). Thus we must construct a uniformly-valid expansion about these boundaries which are then seen as Fresnel regions emanating from the nose of the aerofoil. To evaluate the behaviour in these regions further we must expand about the pole and saddle point, and consider an integration contour that is a small line segment tangent to the steepest descent contour at the point of stationary phase (in the direction of steepest descent). Near to the saddle point, $\lambda = \lambda_0 = -w\cos\theta$, we can approximate the phase function by a Taylor series, hence using the change of variables

$$\lambda + w\cos\theta = \left(\frac{2w\sin^2\theta}{R}\right)^{1/2} \mathrm{e}^{-\pi\mathrm{i}/4} v, \tag{2.2.1.6}$$

we can write

$$H_0 = -\frac{\mathrm{i}\sin\chi\,\mathrm{sgn}(\psi)\mathrm{e}^{\mathrm{i}kwr}}{2\pi\sqrt{\cos\chi+1}\sqrt{(1-\cos\theta)}} \int_{C'} \frac{\mathrm{e}^{-v^2} dv}{v - \beta\mathrm{e}^{-3\pi\mathrm{i}/4}}, \tag{2.2.1.7a}$$

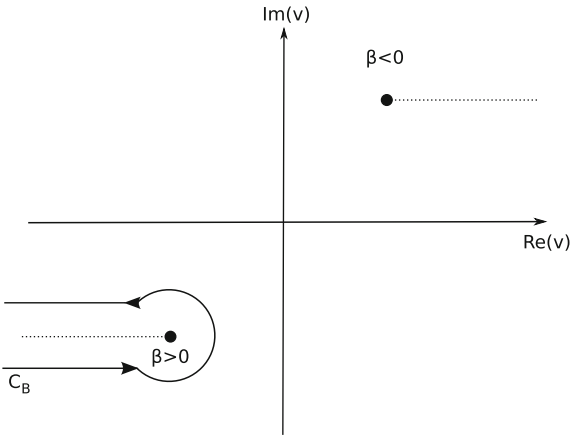

Fig. 2.3 Location of the branch cut of $\sqrt{v - \beta\mathrm{e}^{-3\pi\mathrm{i}/4}}$ in the v-plane, and contour C_B

where

$$\beta = (\cos\chi - \cos\theta)\sqrt{\frac{wR}{2\sin^2\theta}}, \tag{2.2.1.7b}$$

and C' is the straight line from $-\infty e^{\pi i/4}$ to $\infty e^{\pi i/4}$. There are now two distinct limits, namely $\beta = O(1)$ and $\beta \gg 1$. For $\beta \gg 1$ we return to the original limit, whereas for $\beta = O(1)$, consider

$$I = \int_{-\infty}^{\infty} \frac{e^{-v^2 x}}{v - \beta e^{-3\pi i/4}} dv. \tag{2.2.1.8}$$

By solving a first order PDE for $I(x)$ and ensuring that when we deform the contour C' to the real axis to give (2.2.1.8) we go around the pole and include its residue, we find that

$$H_0{}^u \sim \frac{-\sin(\chi)\,\mathrm{sgn}(\psi) e^{ikwr} e^{-i\beta^2}}{2\sqrt{1+\cos\chi}\sqrt{1-\cos\theta}} \mathrm{sgn}(\beta)\mathrm{erfc}\left[e^{-\pi i/4}|\beta|\right] + H_0^p, \tag{2.2.1.9}$$

This is continuous in θ, and now has no singularities; we note in particular that the square root term, $(1-\cos\theta)^{-1/2}$, does not cause any problems as $\theta \to 0$ since the expansion of the complementary error function as $\beta \to \infty$ removes the singularity. The uniformly-valid solution consists of two different acoustic forms, the first term in (2.2.1.9) represents scattering of the incident sound wave by interaction with the edge of the flat plate and away from $\cos\theta = \cos\chi$ takes a cylindrically decaying form, whilst the second term represents direct blocking and reflection of the incident sound wave, and takes the form of a plane wave.

2.2.2 Solution for the Thickness-Related Term H_1

At this order, we begin to take account of the thickness of the aerofoil. We have separated the leading-order correction term in (2.2.0.3) so that we may apply different physical interpretations to each term, and solve the problem more easily. H_1 is therefore chosen to represent only the effect of thickness on the boundary condition, and accounts for the (thickness-dependent) evolution of the phase of the incident sound wave. Specifically, H_1 satisfies

$$D(H_1) = 0, \tag{2.2.2.1a}$$

$$\left.\frac{\partial H_1}{\partial \Psi}\right|_{\substack{\Phi>0 \\ \Psi=0\pm}} = -\frac{iwV(\chi)\mathrm{sgn}(\Psi) a e^{iw\cos(\chi)\Phi}}{4\beta_\infty \cos(\chi)\sqrt{\Phi}}. \tag{2.2.2.1b}$$

The boundary condition, (2.2.2.1b), arises from the $O(\epsilon k^{1/2})$ correction in the boundary condition generated only by the incident sound wave, i.e. by the term $\frac{\partial h_I}{\partial \psi}$ in (2.2.0.2b).

Equation (2.2.2.1) has solution

$$H_1 = \frac{e^{i\pi/4} i w V(\chi) a}{8\sqrt{\pi}\beta_\infty \cos\chi} \int_{-\infty}^{\infty} \frac{e^{-i\lambda\Phi - |\Psi|\sqrt{\lambda^2 - w^2}}}{\sqrt{\lambda^2 - w^2}\sqrt{\lambda + w\cos\chi}} d\lambda. \tag{2.2.2.2}$$

Using the method of steepest descents, we find that in terms of outer variables,

$$H_1 \sim L_1(\theta) \frac{e^{ikwr}}{\sqrt{kr}} + O(k^{-3/2}), \tag{2.2.2.3a}$$

where

$$L_1 = -\frac{V(\chi) a}{4\sqrt{2}\beta_\infty \cos\chi \sqrt{\cos\chi - \cos\theta}}. \tag{2.2.2.3b}$$

The non-uniformity in $L_1(\theta)$ at the points $\cos\chi = \cos\theta$ is caused by the collision of the branch point (as opposed to a pole) at $\lambda = -w\cos\chi$ and the saddle point, $\lambda_0 = -w\cos\theta$, and hence the uniformly-valid contribution differs from the usual Fresnel region solution (caused by the collision of a pole and the saddle point) that was demonstrated in the H_0 solution. Rather than picking up a residue contribution as we deform to the path of steepest descents (such as H_0^p from (2.2.1.5)), we wrap the steepest descents contour around the branch cut between $-w\cos\chi$ and infinity. The branch cut dominates the integral for $\cos\theta$ close to $\cos\chi$ since here the point of stationary phase coalesces with the branch point.

To evaluate the branch cut contribution, we apply the same change of variables, (2.2.1.6), to the original integral expression of H_1, given by (2.2.2.2), to obtain

$$H_1^u \sim c(\theta) \int_{C''} \frac{e^{-v^2}}{\sqrt{v - \beta e^{-3\pi i/4}}} dv \equiv c(\theta) I, \tag{2.2.2.4}$$

where β is still defined by (2.2.1.7b). For $\beta = O(1)$, the contour C'' is wrapped around the branch cut at $\beta e^{-3\pi i/4}$, i.e. is given by C_B shown in Fig. 2.3 when $\beta > 0$. For $|\beta| \gg 1$, the contour, C'' is the standard contour we would obtain via the method of steepest descents (because there is no coalescence of the saddle point and the branch point), which is the contour from $-\infty$ to ∞ along the real axis. Therefore for $|\beta| \gg 1$ we return to the original limit, (2.2.2.3b).

For $\beta > 0$, evaluating the resulting integral around C_B, referring to Abramowitz and Stegun (1964, p. 687), yields

$$I = \int_{C_B} \frac{e^{-v^2}}{\sqrt{v - \beta e^{-3\pi i/4}}} dv = \sqrt{-\beta e^{-3\pi i/4}}\, i K_{1/4}(\beta^2 i/2) e^{i\beta^2/2}, \tag{2.2.2.5}$$

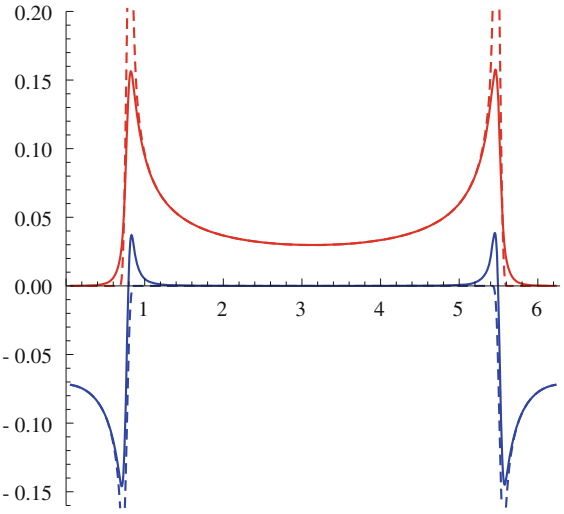

Fig. 2.4 Comparison of real (*red*) and imaginary (*blue*) parts of the uniformly-valid (*solid*) and non uniformly-valid (*dashed*) far-field approximations for the directivity of H_1, as functions of θ, at $kr = 100$. (Color figure online)

where $K_{1/4}(x)$ is a modified Bessel function of the second kind. For $\beta < 0$ we reverse the sign of v within the integral expression for I given in (2.2.2.5), and proceed as before to obtain a similar result.

Therefore the uniformly-valid expansion of H_1 is

$$H_1^u = -\frac{e^{\pi i/4}\sqrt{w}V(\chi)a\,\mathrm{sgn}(\beta)\sqrt{\cos\chi - \cos\theta}}{8\beta_\infty \cos\chi\sqrt{\pi}|\sin\theta|}K_{1/4}(\beta^2 i/2)e^{ikwr}e^{i\beta^2/2}. \tag{2.2.2.6}$$

In the limit of large β this returns to the initial far-field expansion, (2.2.2.3b). For $kr = 100$, Fig. 2.4 illustrates the uniformly-valid expression versus the non-uniformly valid solution. A discussion of this type of uniformly-valid solution can be found in Bleistein and Handelsman (1975).

2.2.3 Solution for the Thickness-Related Term H_2

Tsai (1992) constructs H_2 as the solution that arises due to a source term in the governing equation. We do not have such a source term in (2.2.0.2a), because the incident sound wave does not create any upstream vortical perturbations in our linearised system (an incident gust does of course produce upstream vorticity), hence there is no need for the H_2 term as defined by Tsai (1992). We do, however, have an awkward boundary condition arising from the non-uniform flow around the nose of the aerofoil. We let H_2 be the function that solves for this, i.e. H_2 accounts for the distortion of the mean flow around the aerofoil nose, so

$$D(H_2) = 0, \qquad \left.\frac{\partial H_2}{\partial \Psi}\right|_{\substack{\Phi>0 \\ \Psi=0\pm}} = \frac{-M_\infty^2}{t'\sqrt{k}} \frac{\partial q}{\partial \Psi}(\Phi, 0) \mathrm{e}^{\mathrm{i}w\cos(\chi)\Phi}. \tag{2.2.3.1}$$

This boundary condition arises from the $O(tk^{1/2})$ correction in (2.2.0.2b) generated by the interaction of the incident sound wave with the mean flow; the second term on the right hand side of (2.2.0.2b). Again we solve using the Wiener-Hopf method, but this time, due to the boundary condition, the process is more involved. The solution is given by

$$H_2 = \frac{-\mathrm{sgn}(\Psi)}{2\pi} \int_{-\infty}^{\infty} A_+(\lambda) \mathrm{e}^{-\mathrm{i}\lambda\Phi - |\Psi|\sqrt{\lambda^2 - w^2}} d\lambda, \tag{2.2.3.2a}$$

where $A_+(\lambda)$ is to be determined from the Wiener-Hopf equation

$$\sqrt{\lambda + w} A_+(\lambda) - F_+(\lambda) = \frac{D_-(\lambda)}{\sqrt{\lambda - w}} + F_-(\lambda). \tag{2.2.3.2b}$$

The $F_\pm(\lambda)$ are determined via

$$\frac{D_+(\lambda)}{\sqrt{\lambda - w}} = F_+(\lambda) + F_-(\lambda), \tag{2.2.3.2c}$$

with

$$D_+(\lambda) = -\frac{M_\infty^2}{t'\sqrt{k}} \int_0^\infty \frac{\partial q}{\partial \Psi}(x, 0) \Theta(x) \mathrm{e}^{\mathrm{i}w\cos\chi x} \mathrm{e}^{\mathrm{i}\lambda x} dx, \tag{2.2.3.2d}$$

and $\Theta(x)$ is the Heaviside step function. Recall a subscript $\pm$ denotes a function that is analytic in the upper/lower half plane. D_- is an unknown function, given by

$$D_-(\lambda) = \int_{-\infty}^{0} \left.\frac{\partial H_2}{\partial \Psi}\right|_{\Psi=0} \mathrm{e}^{\mathrm{i}\lambda\Phi} d\Phi. \tag{2.2.3.2e}$$

To evaluate A_+ (and therefore H_2) we refer to Jones (1966) and Tsai (1992). Tsai imposes physical Kutta conditions that $H(\Phi, 0_\pm) \sim \pm\sqrt{\Phi}$ for small positive Φ, and $\left.\frac{\partial H_2}{\partial \Psi}\right|_{\Psi=0} \sim (-\Phi)^{-1/2}$ for small negative Φ. We impose the same conditions, therefore, by relating small Φ behaviour to large λ behaviour, we know that

$$A_+(\lambda) \sim \lambda^{-3/2}, \quad D_+(\lambda) \sim \lambda^{1/2}, \quad \text{and} \quad D_-(\lambda) \sim \lambda^{-1/2} \tag{2.2.3.2f}$$

as $\lambda \to \infty$ in the appropriate half planes. By considering (2.2.3.2c) we see that $F_+ + F_- \sim$ const. as $\lambda \to \infty$. Due to the Kutta conditions imposed for small Φ values, we require $F_+ \to 0$ as $\lambda \to \infty$, so this constant only lies within F_-. The left hand side of Eq. (2.2.3.2b) is analytic in the upper half plane, whilst the right hand

side is analytic in the lower half plane. Both sides have a small region of overlap (allowed by giving w a small positive imaginary part), and for large λ both sides tend to a constant. Therefore both sides give an entire function, which by Liouville's theorem (Noble 1998), must be a constant. We have therefore determined A_+ up to a constant as

$$A_+(\lambda) = \frac{F_+(\lambda) + \text{const.}}{\sqrt{\lambda + w}}. \tag{2.2.3.2g}$$

We can choose to insert the constant into the function F_+ and write

$$F_+(\lambda) = \frac{1}{2\pi \mathrm{i}} \int_{C_1} \frac{D_+(\lambda) + C\sqrt{\lambda - w}}{\sqrt{\kappa - w}} \frac{d\kappa}{\kappa - \lambda}, \tag{2.2.3.2h}$$

where C_1 is a contour running parallel to but just above the real axis, and below w. The constant, C, is determined by ensuring that H_2 behaves in agreement with our restrictions imposed on its small Φ behaviour.

We therefore choose $C = -M_\infty^2 a \mathrm{i}\sqrt{\pi}\beta_\infty^{-1} \mathrm{e}^{\pi \mathrm{i}/4}$ by consulting Jones (1966, p. 468 Ex. 28), and after taking the outer limit of (2.2.3.2a) using the method of steepest descents we obtain

$$H_2 \sim L_2(\theta) \frac{\mathrm{e}^{\mathrm{i}kwr}}{\sqrt{kr}} + O(k^{-3/2}), \tag{2.2.3.3a}$$

where

$$L_2(\theta) = \frac{-a \operatorname{sgn}(\Psi) M_\infty^2 \cos\theta/2}{\beta_\infty \sqrt{\pi}} \left(\tilde{\gamma} + \log[(\cos\chi + 1)w] + 2 - \pi\mathrm{i} \right.$$
$$\left. - 2\mathrm{i} \frac{\sqrt{(\cos\chi - \cos\theta)}}{\sqrt{(1 + \cos\theta)}} \arcsin\left[\frac{\sqrt{(1 + \cos\theta)}}{\sqrt{\cos\chi + 1}} \right] \right), \tag{2.2.3.3b}$$

and $\tilde{\gamma}$ is the Euler-Mascheroni constant. Although it may appear that (2.2.3.2a) has a branch point colliding with the saddle point to produce a non-uniformity, as it did for H_1, in fact this is not the case because the function $F_+(\lambda)$ ensures regular behaviour at the saddle point. The solution presented for L_2 varies from that presented in Ayton and Peake (2013), where the term $-\pi\mathrm{i}$ was given as $-\pi\mathrm{i}/2$.

This Wiener-Hopf method is slightly more complicated that the standard method used in Myers and Kerschen (1997), Tsai (1992) and the previous sections here, because for those, $F_\pm \to 0$ as $\lambda \to \infty$ due to differing boundary conditions, hence they effectively had $C = 0$.

2.2.4 Solution for the Thickness-Related Term H_3

The contribution H_3 arises from terms in (2.2.0.2a) that contain $\epsilon q(\phi, \psi)$, i.e. the effects of the non-uniform flow near the nose on the propagation of the sound through that region. The equation can be rearranged so that the interaction of $\epsilon q(\phi, \psi)$ is seen as an equivalent source term located at the leading edge; this is called a propagation source (Tsai 1992), and so H_3 satisfies

$$D(H_3) = -\frac{2w^2\tilde{a}\beta_\infty \sin\theta/2}{\sqrt{R}}H_0 + \frac{(\gamma+1)M_\infty^4\tilde{a}\sin\theta/2}{\beta_\infty^3\sqrt{R}}\left(\frac{\partial^2 H_0}{\partial\Psi^2} + 2\mathrm{i}\delta\frac{\partial H_0}{\partial\Phi} + (w^2+\delta^2)H_0\right) + \frac{\tilde{a}(\gamma+1)M_\infty^4\sin 3\theta/2}{2\beta_\infty^3 R^{3/2}}\left(\frac{\partial H_0}{\partial\Phi} - \mathrm{i}\delta H_0\right), \tag{2.2.4.1a}$$

$$\left.\frac{\partial H_3}{\partial\Psi}\right|_{\substack{\Phi>0\\ \Psi=0}} = \frac{M_\infty^2\tilde{a}}{2\beta_\infty\Phi^{3/2}}H_0, \tag{2.2.4.1b}$$

where $\tilde{a} = \mathrm{sgn}(\Psi)a$. This final boundary condition arises from the second terms on the left hand side of (2.2.0.2b). The particular solution to (2.2.4.1) is solved for in Appendix 2.8, and has outer limit

$$H_{3p} \sim \frac{a\sqrt{w}\beta_\infty \sin\chi\, \mathrm{e}^{-\mathrm{i}\pi/4}\sin\theta \mathrm{e}^{\mathrm{i}wkr}}{\sqrt{\pi}\sqrt{\cos\chi+1}(\cos\chi-\cos\theta)}\left(1 - \frac{(\gamma+1)M_\infty^4}{2\beta_\infty^4 w^2}(\delta - w\cos\theta)^2\right), + L_{3p}(\theta)\frac{\mathrm{e}^{\mathrm{i}wkr}}{\sqrt{kr}} + O(k^{-1}), \tag{2.2.4.2a}$$

where

$$L_{3p}(\theta) = \frac{-a\sin\chi(\gamma+1)M_\infty^4}{2\sqrt{2}\beta_\infty^3 w\sqrt{\cos\chi+1}}\left(\frac{w}{2}\sin 2\theta - \delta\sin\theta\right). \tag{2.2.4.2b}$$

We do not calculate a uniformly-valid solution for H_{3p}, since the term creating the non-uniformity when $\cos\chi - \cos\theta = 0$ is not present in the outer solution; it is only required for matching the leading-edge inner solution to the leading-edge outer solution.

We now seek a complementary solution, H_{3c}, to (2.2.4.1a) such that $H_3 = H_{3p} + H_{3c}$, with

$$D(H_{3c}) = 0, \tag{2.2.4.3a}$$

$$\left.\frac{\partial H_{3c}}{\partial\Psi}\right|_{\substack{\Phi>0\\ \Psi=0}} = d(\Phi), \tag{2.2.4.3b}$$

where

$$d(\Phi) = \frac{M_\infty^2 a}{2\beta_\infty \Phi^{3/2}} \mathrm{e}^{\mathrm{i}w\cos(\chi)\Phi} \mathrm{erf}\left[\mathrm{e}^{\pi \mathrm{i}/4}\sqrt{(\cos\chi - 1)w\Phi}\right] - \left.\frac{\partial H_{3p}^*}{\partial \Psi}\right|_{\substack{\Phi>0 \\ \Psi=0}}. \tag{2.2.4.3c}$$

The first term in (2.2.4.3c) arises from the uniform expansion of H_0, (2.2.1.9), in the original boundary condition (2.2.4.1b), while the second term is introduced to cancel the normal velocity of the particular solution H_{3p} and is defined in Appendix 2.8. The full expansion for $d(\Phi)$ is given in Appendix 2.9, written in the form

$$d(\Phi) = d_1(\Phi) + d_2(\Phi) + d_3(\Phi)$$

so as to simplify later calculations. We set

$$H_{3c} = \Sigma_{i=1}^{3} H_{3c_i}, \tag{2.2.4.4a}$$

where each H_{3c_i} corresponds to the term d_i in the boundary condition (2.2.4.3b). The solution to (2.2.4.3) can be obtained using the Wiener-Hopf method, giving

$$H_{3c_i} = -\frac{\mathrm{sgn}(\Psi)}{2\pi} \int_{-\infty}^{\infty} F_{+i}(\lambda) \frac{\mathrm{e}^{a(\lambda,\Phi,\Psi)}}{\sqrt{\lambda + w}} d\lambda, \tag{2.2.4.4b}$$

where the F_{+i} are also given in Appendix 2.9. In the limit of large R, we obtain

$$H_{3c_i} \sim L_{3c_i}(\theta) \frac{\mathrm{e}^{\mathrm{i}wkr}}{\sqrt{kr}} + O(k^{-3/2}), \quad \text{for } i = 1, 2, 3, \tag{2.2.4.5}$$

where the expressions for the L_{3c_i}, and their uniformly-valid counterparts, can be found in Appendix 2.9.

2.2.5 *Solution for the Camber-Related Terms P_i, $i = 1, 2, 3$*

Recall that the P_i terms in (2.2.0.3) are the components of the inner solution that correspond to the leading-edge effects of camber and angle of attack on the scattering of the incident sound wave. The P_1 solution comes from the differentiation of the integral in the exponent of h_I, given by (2.1.3.7), within the boundary condition (i.e. the effect of the cumulative distortion of the sound wave as it propagates through the non-uniform mean flow on the incident normal velocity) and so satisfies

$$D(P_1) = 0, \tag{2.2.5.1a}$$

$$\left.\frac{\partial P_1}{\partial \Psi}\right|_{\substack{\Phi>0 \\ \Psi=0\pm}} = -\frac{\mathrm{i}wV(\chi)\mathrm{sgn}(\Psi)\mathrm{e}^{\mathrm{i}w\cos\chi\,\Phi}}{2\sqrt{2}\beta_\infty \sin\chi\sqrt{\Phi}}. \tag{2.2.5.1b}$$

Again, using the Wiener-Hopf technique in a standard way, we find that

$$P_1 = \frac{e^{i\pi/4} i w V(\chi)}{4\sqrt{2\pi}\beta_\infty w \sin\chi} \int_{-\infty}^{\infty} \frac{e^{-i\lambda\Phi - |\Psi|\sqrt{\lambda^2 - w^2}}}{\sqrt{\lambda^2 - w^2}\sqrt{\lambda + w\cos\chi}} d\lambda, \tag{2.2.5.1c}$$

and a uniformly-valid outer limit can be found using the method described in Sect. 2.2.2, giving

$$P_1^u = -\frac{e^{\pi i/4}\sqrt{w} V(\chi)\mathrm{sgn}(\beta)\sqrt{\cos\chi - \cos\theta}}{4\sqrt{2\pi}\beta_\infty \sin\chi |\sin\theta|} K_{1/4}(\beta^2 i/2) e^{ikwr} e^{i\beta^2/2}. \tag{2.2.5.1d}$$

The H_2 term in (2.2.0.3) arose from the influence of the thickness-dependent part of the mean velocity potential in the boundary condition (2.2.0.2b) (i.e. the term containing q), however the camber-dependent part of the potential tells us that this term is zero, and hence we set $P_2 = 0$.

The term P_3 in (2.2.0.3) arises from the terms involving q in (2.2.0.2a) forming a source term in a similar way to the propagation source for H_3, namely

$$D(P_3) = \frac{\sqrt{2}}{\beta_\infty\sqrt{R}} \cos\frac{\theta}{2} \left(2\beta_\infty^2 w^2 H_0 - \frac{(\gamma+1)M_\infty^4}{\beta_\infty^2} \left[\frac{\partial^2 H_0}{\partial\Psi^2} + 2i\delta \frac{\partial H_0}{\partial\Phi} + (w^2 + \delta^2) H_0 \right] \right) - \frac{1}{R^{3/2}} \cos\frac{3\theta}{2} \frac{(\gamma+1)M_\infty^4}{\sqrt{2}\beta_\infty^3} \left[\frac{\partial H_0}{\partial\Phi} - i\delta H_0 \right], \tag{2.2.5.2a}$$

$$\frac{\partial P_3}{\partial\Psi}\Big|_{\substack{\Phi>0 \\ \Psi=0\pm}} = 0. \tag{2.2.5.2b}$$

The boundary condition is zero normal derivative since the Ψ derivative of the part of q corresponding to the leading-edge camber and angle of attack is zero on the aerofoil. Hence we can use a modified form of the solution for the gust case from Myers and Kerschen (1997); setting $P_3 = P_{3c} + P_{3p} + P_{3e}$, gives

$$P_{3p}(R,\theta) = iw\sqrt{2kr} \left(-2\beta_\infty + \frac{(\gamma+1)M_\infty^4}{\beta_\infty^3 w^2} (\delta - w\cos\theta)^2 \right) \cos\frac{\theta}{2} H_0, \tag{2.2.5.3a}$$

$$P_{3c}(R,\theta) = \frac{iw\sin\chi\,\beta_\infty e^{\pi i/4}}{\sqrt{2\pi}} \int_{-\infty}^{\infty} \left(\frac{1}{\sqrt{\lambda+\delta}} - \frac{\delta}{(\lambda+\delta)^{3/2}} \right) \frac{e^{a(\lambda,\phi,\psi)}}{\sqrt{\lambda^2 - w^2}} d\lambda, \tag{2.2.5.3b}$$

$$P_{3e}(R,\theta) = \frac{-\sqrt{2\pi}(\gamma+1)M_\infty^2 iw\sin\chi\, e^{-i\pi/4}}{8\beta_\infty^3\sqrt{\delta+w}} \left(H_2^{(1)}(wR)\cos 2\theta + \frac{2i\delta}{w} H_1^{(1)}(wR)\cos\theta \right). \tag{2.2.5.3c}$$

The modification to Myers and Kerschen's result arises in the first factor within the integrand of P_{3c}. The outer limit of $P_{3c} + P_{3e}$ is

$$P_{3c} + P_{3e} \sim D_3(\theta) \frac{e^{ikwr}}{\sqrt{kr}} + O(k^{-3/2}), \tag{2.2.5.3d}$$

where

$$D_3(\theta) = \frac{w^{3/2}\beta_\infty \sin\chi\cos\theta}{(\delta - w\cos\theta)^{3/2}} - \frac{(\gamma+1)M_\infty^4 \sin\chi}{\sqrt{w}\sqrt{\delta+w}\beta_\infty^3}\left(\frac{\delta}{2}\cos\theta - \frac{w}{4}\cos 2\theta\right). \tag{2.2.5.3e}$$

We have thereby now completed our asymptotic solution in the inner region, and have crucially found a uniformly-valid outer limit which can be matched onto the solution in the outer region.

2.3 Solution for the Leading-Edge Outer and Transition Regions

We first solve for the boundary condition, (2.1.3.8), in the outer region. Clearly, $-h_I$ is a solution in the outer region, however we need to construct an outer solution, h^o, that matches to an appropriate function in the leading-edge inner limit, but also cancels the normal velocity of h_I on the aerofoil surface. The appropriate function for $\psi > 0$ is

$$h^o = \mathrm{e}^{\mathrm{i}wk\cos\chi\,\phi + \mathrm{i}wk\sin\chi\,|\psi| + \mathrm{i}kw\epsilon\sigma_1(\tilde{\xi},\tilde{\eta})}\left(\Theta(\theta_t) - \Theta(\theta_t - \chi) - \Theta(\theta) + \Theta(\theta - \chi)\right), \tag{2.3.0.1}$$

where σ_1 is defined in (2.1.3.5), and $\tilde{\xi} = \phi + \cot\chi|\psi|$, $\tilde{\eta} = \phi - \cot\chi|\psi|$. The Heaviside step functions, Θ, dictate that h^o is only non-zero if an observer is in the direct shadow which is defined by the polar angle measured from the leading edge satisfying $\theta \in (0, \chi)$, and the polar angle measured from the trailing edge satisfying $\theta_t \in (0, \chi)$. For $\psi < 0$ we require a reflected solution given by

$$h^o = -\mathrm{e}^{\mathrm{i}wk\cos\chi\,\phi + \mathrm{i}wk\sin\chi\,|\psi| + \mathrm{i}kw\epsilon\sigma_1(\tilde{\xi},\tilde{\eta})}\left[\Theta(-\theta_t) - \Theta(-\theta_t - \chi)\right. \\ \left. -\Theta(\theta - (2\pi - \chi)) + \Theta(\theta - 2\pi)\right]. \tag{2.3.0.2}$$

In the far field, these regions reduce to a small, $O(1/r)$, polar regions near $\theta = \chi$, $2\pi - \chi$, which coincide with the location of the shadow and reflection boundaries around which the Fresnel regions are centred. In the leading-edge inner limit, the terms from the $(-\Theta(\theta) + \Theta(\theta - \chi))$ contributions match to the outer limit of the inner leading-edge term, H_0^p, given by (2.2.1.5). The other terms, from the $\Theta(\theta_t) - \Theta(\theta_t - \chi)$ contributions, will match to a trailing-edge inner solution which comes from another pole contribution.

At distances of $r = O(k)$ in the far field, the scattered Fresnel regions emanating from the leading and trailing edges overlap and eclipse this h^o term, similar to the case seen in Peake and Kerschen (2004), thus in the far field we do not actually see h^o.

2.3.1 Leading-Edge Ray Field

The leading-edge ray field (which is a scattered solution) is analogous to the gust cases found in Tsai (1992) and Myers and Kerschen (1997), so we propose a cylindrically decaying leading-edge outer solution of the form

$$h_l = \frac{K_0(\theta) + t\sqrt{k}K_1(\theta) + \alpha_{\text{eff}}\sqrt{k}K_2(\theta)}{\sqrt{kr}} \mathrm{e}^{\mathrm{i}kw\sigma_l(r,\theta)}. \tag{2.3.1.1a}$$

We substitute (2.3.1.1a) into (2.1.2.4) to give the eikonal equation for σ_l, and solving up to and including $O(\epsilon)$, we obtain

$$\sigma_l = r + \epsilon\sigma_{l_1} + O(\epsilon^2), \tag{2.3.1.1b}$$

where

$$\sigma_{l_1} = V(\theta)\int_0^r q(r',\theta)dr' + \sigma_1(0,0), \tag{2.3.1.1c}$$

and V is defined in (2.1.3.6). We finally obtain the solutions to K_i by Van Dyke's matching rule (Van Dyke 1975), whereby we match the outer limit ($R \to \infty$) of the inner solution (2.2.0.3) onto the inner limit ($r \to 0$) of the outer solution (2.3.1.1a). Hence, similarly to Myers and Kerschen (1997) and Tsai (1992),

$$K_0(\theta) = L_0(\theta), \tag{2.3.1.1d}$$

$$K_1(\theta) = L_1(\theta) + L_2(\theta) + L_{3p}(\theta) + L_{3c_1}(\theta) + L_{3c_2}(\theta) + L_{3c_3}(\theta), \tag{2.3.1.1e}$$

$$K_2(\theta) = D_1(\theta) + D_2(\theta) + D_3(\theta), \tag{2.3.1.1f}$$

in the non uniformly-valid case. The cross-term from the inner limit of h_l, given by $K_0(\theta)\mathrm{i}kw\epsilon V(\theta)\int_0^r q dr'$, matches to the first term in the particular solution, H_{3p} from (2.2.4.2a), and to P_{3p} from (2.2.5.3a). For a uniformly-valid matching, we must replace the non uniformly-valid terms, (L_0, L_1, L_{3c_1}, L_{3c_2}, D_1) by their uniformly-valid counterparts (e.g. $H_0^u\sqrt{kr}$). This still provides a matching, however the amplitude function is now dependent on r as well as on θ. In all cases that follow, to obtain the uniformly-valid solution we replace any non uniformly-valid terms by their uniformly-valid counterparts in this way. To aid the understanding of the matching problems, results will in general be given in terms of non uniformly-valid solutions where appropriate.

2.3.2 Leading-Edge Transition Solution

When finding the leading-edge outer scattered solution we did not impose a boundary condition on the aerofoil surface, and furthermore the expansion of L_{3c_2} becomes

non uniform at small angles (illustrated by the logarithmic singularity in (2.9.0.8) at $\lambda = -w$). These two issues lead us to look for a boundary-layer style solution, which emanates from the leading edge and is valid close to the aerofoil surface, that cancels the normal velocity generated by the leading-edge outer ray field. When $\theta = O(k^{-1/2})$, and $r = O(1)$, there is a distinguished limit in the integral term in $L^u_{3c_2}$, (2.9.0.10), giving a boundary-layer style structure to our leading-edge inner solution. We therefore seek a complementary solution, h_{ls}, that is exponentially small outside a region of width $O(k^{-1/2})$ on the aerofoil surface. In this case, the matching previously done of H onto h_l is still valid, and we can write the total leading-edge solution as

$$h^u_l = h_l + h_{ls}. \tag{2.3.2.1}$$

We do, however, require an explicit expression for this transition solution in order to evaluate the pressure jump it creates at the trailing edge of the aerofoil. We then also require a suitable complementary function around the trailing edge to ensure the pressure is continuous across the wake, i.e. the Kutta condition is satisfied.

We know that h_{ls} must still satisfy governing equation (2.1.2.4), and it must have boundary condition

$$\frac{\partial h_{ls}}{\partial \psi} + M_\infty^2 \epsilon \frac{\partial q}{\partial \psi} h_{ls}\bigg|_{\psi=0_\pm} = -\frac{\partial h_l}{\partial \psi} - M_\infty^2 \epsilon \frac{\partial q}{\partial \psi} h_l\bigg|_{\psi=0_\pm} \tag{2.3.2.2}$$

to ensure zero normal velocity on both upper and lower blade surfaces. On the upper surface we introduce a rescaled variable $\eta = \sqrt{k}\psi$ to represent this boundary layer structure. We can once again consider the thickness-dependent terms and camber-dependent terms separately, denoting the thickness-dependent part of the mean velocity perturbation, ϵq, as $\epsilon q^{(t)}$ and similarly the camber-dependent part as $\epsilon q^{(c)}$. We begin with the thickness dependent terms hence follow the method set out by Tsai (1992). By balancing terms in the boundary condition (2.3.2.2), we consider a solution of the form

$$h^{(t)}_{ls}(\phi, \eta) = t\mathcal{G}(\phi, \eta) \mathrm{e}^{\mathrm{i}kw\phi + \mathrm{i}kw\epsilon V(0) \int_0^r q(r',0)dr' + \mathrm{i}kw\epsilon\sigma_1(0,0)}, \tag{2.3.2.3}$$

so to leading order, (2.1.2.4) becomes

$$2\mathrm{i}w\frac{\partial \mathcal{G}}{\partial \phi} + \frac{\partial^2 \mathcal{G}}{\partial \eta^2} = 0. \tag{2.3.2.4a}$$

The boundary condition is applied along the whole of $\phi > 0$; we deduct the $\phi > 2$ part that we don't require later in Sects. 2.4.2 and 2.4.3 as part of the trailing-edge transition solution. We therefore require

$$\frac{\partial \mathcal{G}}{\partial \eta}\bigg|_{\eta=0} = b(\phi), \tag{2.3.2.4b}$$

where

$$b(\phi) = \frac{e^{-i\pi/4}V(0)}{\sqrt{\pi}\beta_\infty\sqrt{\cos\chi+1}}\frac{\sqrt{w}\sin\chi}{1-\cos\chi}\frac{1}{\phi}\left(\frac{\beta_\infty}{t'\sqrt{\phi}}\int_0^\phi \frac{\partial q^{(t)}}{\partial\theta}(r',0)dr' + a\right) \tag{2.3.2.4c}$$

for $0 < \phi < 2$, and

$$b(\phi) = \frac{e^{-i\pi/4}V(0)}{\sqrt{\pi}\beta_\infty\sqrt{\cos\chi+1}}\frac{\sqrt{w}\sin\chi}{1-\cos\chi}\frac{1}{\phi}\left(\frac{\beta_\infty}{t'\sqrt{\phi}}\int_0^2 \frac{\partial q^{(t)}}{\partial\theta}(r',0)dr' + a\right) \tag{2.3.2.4d}$$

for $\phi > 2$.

By using the Laplace transform with respect to the variable η in (2.3.2.4a) and applying the required boundary condition, we find that

$$\mathcal{G}(\phi,\eta) = \frac{V(0)\sin\chi}{\sqrt{2}\beta_\infty\pi\sqrt{\cos\chi+1}(\cos\chi-1)}\int_0^\phi\left[\frac{a}{\xi}+\frac{\beta_\infty}{t'\xi^{3/2}}\int_0^\xi\frac{\partial q^{(t)}}{\partial\theta}(r',0)dr'\right]\frac{e^{i\eta^2 w/2(\phi-\xi)}}{\sqrt{\phi-\xi}}d\xi \tag{2.3.2.5a}$$

for $0 < \phi < 2$, and

$$\begin{aligned}\mathcal{G}(\phi,\eta) = &\frac{V(0)\sin\chi}{\sqrt{2}\beta_\infty\pi\sqrt{\cos\chi+1}(\cos\chi-1)}\left(\int_0^2\left[\frac{a}{\xi}+\frac{\beta_\infty}{t'\xi^{3/2}}\int_0^\xi\frac{\partial q^{(t)}}{\partial\theta}(r',0)dr'\right]\frac{e^{i\eta^2 w/2(\phi-\xi)}}{\sqrt{\phi-\xi}}d\xi\right.\\ &\left.+\int_2^\phi\left[\frac{a}{\xi}+\frac{\beta_\infty}{t'\xi^{3/2}}\int_0^2\frac{\partial q^{(t)}}{\partial\theta}(r',0)dr'\right]\frac{e^{i\eta^2 w/2(\phi-\xi)}}{\sqrt{\phi-\xi}}d\xi\right)\end{aligned} \tag{2.3.2.5b}$$

for $\phi > 2$ (this will be used to find the pressure jump reaching the trailing edge). On the lower surface, $\psi = 0_-$, we apply the same theory as for the upper surface, but using instead the transform variable $\eta = -\sqrt{k}\psi$.

The camber-dependent transition solution is similar to that found in Myers and Kerschen (1997) with appropriate redefinition of terms, so in the far-field limit takes the form

$$h_{ls}^{(c)} \sim \frac{e^{ikw\phi+ikw\epsilon V(0)\int_0^r q(r',0)dr'+ikw\epsilon\sigma_1(0,0)}}{\sqrt{r}}D_{ltr}(\theta), \tag{2.3.2.6a}$$

$$\begin{aligned}D_{ltr}(\theta) = \mathrm{sgn}(\psi)\frac{e^{3i\pi/4}\epsilon V(0)}{\sqrt{2w\pi}\beta_\infty}P_l(0_\pm)\left[\int_0^2 e^{ikw(1-\cos\theta)\xi}\left(\xi^{-1/2}y^{(c)\prime}(\xi)-\xi^{-3/2}y^{(c)}(\xi)\right)d\xi\right.\\ \left.+2^{3/2}y^{(c)\prime}(2)\left(e^{2ikw(1-\cos\theta)}-\sqrt{\pi}e^{-\pi i/4}\sqrt{2kw(1-\cos\theta)}\mathrm{erfc}\left(e^{-\pi i/4}\sqrt{2kw(1-\cos\theta)}\right)\right)\right].\end{aligned} \tag{2.3.2.6b}$$

$$P_l(\theta) = \left[L_0(\theta)+\alpha_{\mathrm{eff}}\sqrt{k}\,(D_1(\theta)+D_2(\theta)+D_3(\theta))\right]. \tag{2.3.2.6c}$$

The overall order of the camber-dependent transition solution is $O(\epsilon)$, like the thickness-dependent transition solution. We have now completed our description of the solution in the transition region. The total leading-edge transition solution (both thickness- and camber-dependent parts) is consistent with the leading-edge inner and outer solutions because in both limits the transition solution tends to zero except at small angles downstream (where $\theta \approx 0, 2\pi$) in the far-field limit. The difference at these small angles does not invalidate our current solutions because we correct these differences with trailing-edge solutions later.

We can now determine the total far-field sound scattered from the leading edge, given by (2.3.2.1), which for large r is

$$\begin{aligned} h_l^u(r,\theta) \sim \frac{\mathrm{e}^{\mathrm{i}kw\sigma_l(r,\theta)}}{\sqrt{kr}} \Bigg\{ & L_0(\theta) + t\sqrt{k}\Big[L_1(\theta) + L_2(\theta) + L_{3p}(\theta) + L_{3c_1}(\theta) + L_{3c_2}(\theta) \\ & + L_{3c_3}(\theta) - \frac{\operatorname{sgn}(\psi)\sin\chi\beta_\infty}{\sqrt{2}\pi\sqrt{\cos\chi+1}(\cos\chi-1)}\left(1 - \frac{(\gamma+1)M_\infty^4}{2\beta_\infty^4 w^2}(\delta-w)^2\right) \\ & \left(\int_0^2 \left[\frac{a}{\tau} + \frac{\beta_\infty}{t'\tau^{3/2}}\int_0^\tau \frac{\partial q^{(t)}}{\partial\theta}(r',0)dr'\right]\mathrm{e}^{\mathrm{i}wk(1-\cos\theta)\tau}d\tau\right. \\ & \left. + \int_2^\infty \left[\frac{a}{\tau} + \frac{\beta_\infty}{t'\tau^{3/2}}\int_0^2 \frac{\partial q^{(t)}}{\partial\theta}(r',0)dr'\right]\mathrm{e}^{\mathrm{i}wk(1-\cos\theta)\tau}d\tau\right)\Big] \\ & + \alpha_{\mathrm{eff}}\sqrt{k}\left[D_1(\theta) + D_2(\theta) + D_3(\theta)\right] + \sqrt{k}D_{ltr}(\theta)\Bigg\}. \end{aligned} \tag{2.3.2.7}$$

The outer limits of the transition solution has been used in (2.3.2.7). These outer limits only take effect at angles that are within $O(k^{-1/2})$ of $\theta = 0$, which can be

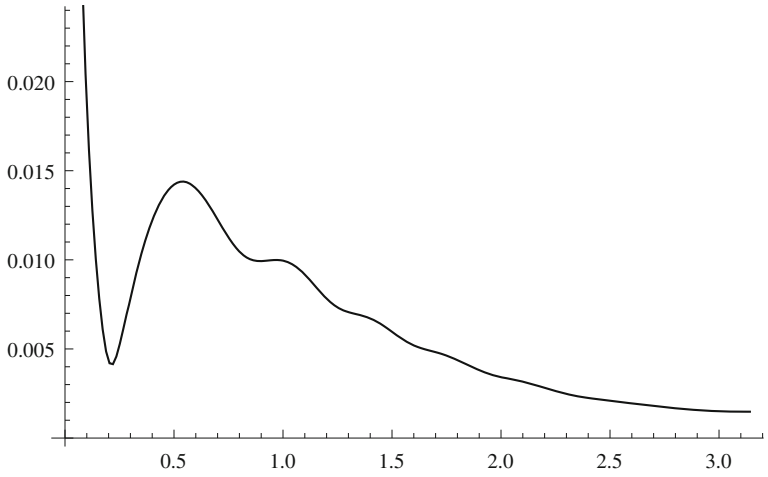

Fig. 2.5 Magnitude of the far-field limit of the leading-edge transition solution (multiplied by $\sqrt{r}$) as a function of polar angle, θ, for a NACA 1112 aerofoil with $k = 10$

seen by considering the small θ expansion of the phase function $kw(1-\cos\theta)$ in the transition terms in (2.3.2.6) and (2.3.2.7). Figure 2.5 illustrates the magnitude of the leading-edge transition solution. The relative size for comparison is $t = 0.12$ which is the order of magnitude of the thickness-related perturbation terms to the leading-edge outer solution (multiplied by $\sqrt{r}$). We clearly see that away from $\theta = 0$ the transition solution is negligible compared to the orders retained in our calculations.

2.4 Solution for the Trailing-Edge Outer, Transition, and Inner Regions

2.4.1 Trailing-Edge Ray Field

Let (ϕ_t, ψ_t) be the potential-streamfunction coordinates with origin shifted to the trailing edge. Since we do not necessarily have a non-lifting aerofoil, ϕ_t changes above and below the aerofoil, so the transformation between leading- and trailing-edge coordinates is given by

$$\phi = 2 \pm \frac{\Gamma}{2} + \alpha_t + \phi_t, \qquad \psi = \psi_t, \tag{2.4.1.1}$$

where Γ is the total circulation around the aerofoil given by

$$\Gamma = \frac{2\pi}{\beta_\infty}\alpha_g, \tag{2.4.1.2}$$

$$\alpha_g = \alpha_i + \frac{1}{\pi}\int_0^2 \frac{\epsilon y^{(c)}(x)}{\sqrt{x}(2-x)^{3/2}}dx, \tag{2.4.1.3}$$

and

$$\alpha_t = \mathrm{Re}(\epsilon F^{(t)}(2)), \tag{2.4.1.4}$$

where $F^{(t)}$ is the thickness-dependent part of the complex potential given by (2.1.1.7). Note that both Γ and α_t are $O(\epsilon)$, given our assumption of thin aerofoils with small camber and angle of attack.

The ray field emanating from the trailing edge is of the same form as in the gust cases of Tsai (1992) and Myers and Kerschen (1997), so we write

$$h_t = \frac{K_t(\theta_t)}{k\sqrt{r_t}} \mathrm{e}^{\mathrm{i}kw\sigma_t(r_t,\theta_t)}, \tag{2.4.1.5a}$$

where (r_t, θ_t) are trailing-edge polar coordinates, and the trailing-edge phase is

$$\sigma_t = r_t + \epsilon\sigma_{t_1} + O(\epsilon^2), \tag{2.4.1.5b}$$

with

$$\sigma_{t_1} = V(\theta_t) \int_0^{r_t} q(r_t', \theta_t) dr_t' + g_2(\theta_t). \tag{2.4.1.5c}$$

The directivity function, $K_t(\theta_t)$, and the phase function, $g_2(\theta_t)$, are as yet unknown, and must be determined by matching with the trailing-edge inner solution.

2.4.2 Trailing-Edge Inner Solution

We move to the trailing-edge coordinate system (2.4.1.1). Letting $(\Phi_t, \Psi_t) = k(\phi_t, \psi_t)$ and $H_t^{\text{tot}}(\Phi_t, \Psi_t)$ be the local inner solution for the trailing edge, the leading-order terms in (2.1.2.4) and (2.1.3.8) are

$$\frac{\partial^2 H_t^{\text{tot}}}{\partial \Phi_t^2} + \frac{\partial^2 H_t^{\text{tot}}}{\partial \Psi_t^2} + w^2 H_t^{\text{tot}} = 0, \tag{2.4.2.1a}$$

$$\left.\frac{\partial H_t^{\text{tot}}}{\partial \Psi_t}\right|_{\substack{\Phi_t<0 \\ \Psi_t=0}} = -\left.\frac{\partial h_I}{\partial \psi}\right|_{\substack{\phi<0 \\ \psi=0}}. \tag{2.4.2.1b}$$

We require the pressure to be continuous across the wake $\psi_t = 0, \phi_t > 0$, where the pressure jump across the wake caused by our leading-edge transition solution is given in Appendix 2.10. We can write the pressure jump as

$$p_l|_{\psi=0+} - p_l|_{\psi=0-} = \Delta p(\phi_t)\sqrt{k}\mathrm{e}^{\mathrm{i}k(w-\delta M_\infty^2)\phi_t}\mathrm{e}^{\mathrm{i}k\epsilon w V(0)[\int_0^\phi q dr - \int_0^2 q dr]}, \tag{2.4.2.2}$$

and later we separate this into contributions from thickness and camber, save for an interaction of the two in phase terms.

We first consider a trailing-edge inner solution, H_t, that cancels the pressure jump, (2.4.2.2), and satisfies (2.4.2.1a). With this solution we also enforce continuity of displacement across the wake,

$$\mathrm{e}^{-\mathrm{i}C_+}\left.\frac{\partial H_t}{\partial \Psi_t}\right|_{\substack{\Phi_t>0 \\ \Psi_t=0+}} = \mathrm{e}^{-\mathrm{i}C_-}\left.\frac{\partial H_t}{\partial \Psi_t}\right|_{\substack{\Phi_t>0 \\ \Psi_t=0-}}, \tag{2.4.2.3}$$

where the constants $C_\pm$ are defined by

$$C_\pm = k\delta M_\infty^2(2 \pm \Gamma/2 + \alpha_t), \tag{2.4.2.4}$$

and the continuity of pressure across the wake imposes

$$\mathrm{e}^{-\mathrm{i}C_-}\left[\frac{\partial H_t}{\partial \Phi_t} - i\delta H_t\right]_{\substack{\Phi_t>0\\ \Psi_t=0-}} - \mathrm{e}^{-\mathrm{i}C_+}\left[\frac{\partial H_t}{\partial \Phi_t} - \mathrm{i}\delta H_t\right]_{\substack{\Phi_t>0\\ \Psi_t=0+}} = \frac{\Delta p(0)}{\sqrt{k}}\mathrm{e}^{\mathrm{i}w\Phi_t}, \tag{2.4.2.5}$$

We do not impose (2.4.2.1b) on H_t since we introduce a further solution, H_t^{ref}, to account for the direct reflection of the incident sound wave by the trailing edge. We therefore require that H_t has zero normal velocity on the aerofoil surface,

$$\left.\frac{\partial H_t}{\partial \Psi_t}\right|_{\substack{\Phi_t<0\\ \Psi_t=0}} = 0. \tag{2.4.2.6}$$

We solve for H_t using the Wiener-Hopf method, to yield

$$H_t = \frac{\mathrm{sgn}(\Psi_t)\mathrm{i}\sqrt{2w}\Delta p(0)\mathrm{e}^{\mathrm{i}C_\pm}}{4\pi\sqrt{k}}\int_{-\infty}^{\infty}\frac{\mathrm{e}^{-\mathrm{i}\lambda\Phi_t - |\Psi_t|\sqrt{\lambda^2-w^2}}}{(\lambda+\delta)(\lambda+w)\sqrt{\lambda-w}}d\lambda. \tag{2.4.2.7a}$$

We must match this solution onto the outer trailing-edge solution, (2.4.1.5), so evaluate (2.4.2.7a) for $R_t \gg 1$. The uniformly-valid expansion, found using Van der Waerden's method (Van der Waerden 1952), is

$$H_t \sim T(r_t,\theta_t)\frac{\mathrm{e}^{\mathrm{i}kwr_t}}{k\sqrt{r_t}}, \tag{2.4.2.7b}$$

where

$$T(r_t,\theta_t) = \frac{\mathrm{sgn}(\psi_t)\mathrm{i}\Delta p(0)\mathrm{e}^{\mathrm{i}C_\pm}}{2(\delta-w)}\left[\mathrm{erfc}(\mathrm{e}^{-\mathrm{i}\pi/4}\sqrt{w(1-\cos\theta_t)kr_t})\mathrm{e}^{\mathrm{i}kwr_t(\cos\theta_t-1)}\sqrt{kr_t}\right.$$
$$\left. - \frac{\sqrt{2w}\mathrm{e}^{\mathrm{i}\pi/4}|\sin\theta_t/2|}{\sqrt{\pi}(\delta - w\cos\theta_t)}\right], \tag{2.4.2.7c}$$

which is similar to the trailing-edge inner solution found by Tsai (1992).

The reflection of the incident sound wave by the aerofoil surface in the trailing-edge region requires us to construct the solution, H_t^{ref}, which we write as

$$H_t^{ref} = H_0^t\mathrm{e}^{\mathrm{i}kw\cos\chi(2\pm\Gamma/2+\alpha_t)+\mathrm{i}kw\epsilon\sigma_1^t(0,0)}, \tag{2.4.2.8}$$

where σ_1^t is just σ_1, from (2.1.3.5), but in trailing-edge coordinates. To leading order, H_0^t must satisfy

$$\frac{\partial^2 H_0^t}{\partial \Phi_t^2} + \frac{\partial^2 H_0^t}{\partial \Psi_t^2} + w^2 H_0^t = 0, \tag{2.4.2.9a}$$

$$\left.\frac{\partial H_0^t}{\partial \Psi_t}\right|_{\substack{\Phi_t<0 \\ \Psi_t=0\pm}} = -\mathrm{i}w \sin\chi \mathrm{e}^{\mathrm{i}w\cos\chi\Phi_t}. \tag{2.4.2.9b}$$

Just as in Sect. 2.2.1, we find that

$$H_0^t \sim L_0^t(\theta_t)\frac{\mathrm{e}^{\mathrm{i}kwr_t}}{\sqrt{kr_t}}, \tag{2.4.2.10a}$$

as $R_t \to \infty$, where

$$L_0^t(\theta_t) = -\frac{\sin\chi \mathrm{e}^{-\pi\mathrm{i}/4}\sin\theta_t/2}{\sqrt{w\pi}\sqrt{1-\cos\chi}(\cos\chi-\cos\theta_t)} + H_0^{t,p}, \tag{2.4.2.10b}$$

where $H_0^{t,p}$ is a pole contribution given by

$$H_0^{t,p} = \mathrm{sgn}\Psi_t \mathrm{e}^{\mathrm{i}w\cos\chi\,\Phi_t + \mathrm{i}w\sin\chi\,|\Psi_t|} \tag{2.4.2.10c}$$

when $-\chi < \theta_t < \chi$, and zero otherwise. The outer limit of this pole contribution matches to the remaining term (that explicitly contains θ_t) in h^o. The equivalent uniformly-valid expansion for (2.4.2.10) is

$$H_0^t \sim \frac{\mathrm{i}\sin\chi \mathrm{e}^{-\mathrm{i}\beta_t^2}\mathrm{e}^{\mathrm{i}kwr_t}\mathrm{sgn}(\Psi_t)}{2\sqrt{1-\cos\chi}\sqrt{1+\cos\theta_t}}\mathrm{sgn}(\beta_t)\mathrm{erfc}\left[\mathrm{e}^{-\pi\mathrm{i}/4}|\beta_t|\right] + H_0^{t,p}, \tag{2.4.2.11}$$

where

$$\beta_t = (\cos\chi - \cos\theta_t)\sqrt{\frac{wR_t}{2\sin^2\theta_t}}. \tag{2.4.2.12}$$

The pole contribution from $H_0^{t,p}$ matches to the outer solution, h^o, given by (2.3.0.1).

By combining (2.4.2.7) and (2.4.2.11), the overall scattered solution (i.e. without the pole term) for the trailing-edge inner region has outer limit

$$\begin{aligned} H_t^{tot} &= H_t + H_0^t \mathrm{e}^{\mathrm{i}kw\cos\chi(2\pm\Gamma/2+\alpha_t)+\mathrm{i}kw\epsilon\sigma_1^t(0,0)} \\ &\sim \left(T(\theta_t) + \sqrt{k}L_0^t(\theta_t)\mathrm{e}^{\mathrm{i}kw\cos\chi(2\pm\Gamma/2+\alpha_t)+\mathrm{i}kw\epsilon\sigma_1^t(0,0)}\right)\frac{\mathrm{e}^{\mathrm{i}kwr_t}}{k\sqrt{r_t}}. \end{aligned} \tag{2.4.2.13}$$

This is matched onto the outer trailing-edge ray field (2.4.1.5) using Van Dyke's matching rule, yielding the final results;

$$K_t(\theta_t) = T(\theta_t) + \sqrt{k} L_0^t(\theta_t) \mathrm{e}^{\mathrm{i}kw\cos\chi(2\pm\Gamma/2+\alpha_t)+\mathrm{i}kw\epsilon\sigma_1^t(0,0)} \quad \text{and} \quad g_2(\theta_t) = 0. \tag{2.4.2.14}$$

2.4.3 Trailing-Edge Transition Solution

We now construct the trailing-edge transition solution h_{ts}, which cancels the pressure jump across the entire wake caused by the leading-edge field. We again split the solution into thickness-dependent, $h_{ts}^{(t)}$, and camber-dependent parts, $h_{ts}^{(c)}$, where the thickness-dependent part of the transition solution remains similar to the gust case of Tsai (1992), save for some rescaling, so

$$h_{ts}^{(t)} = \frac{1}{\sqrt{k}} \mathcal{G}_t(\phi_t, \eta_t) \mathrm{e}^{\mathrm{i}kw\sigma_t(\phi_t,0)}, \qquad \eta_t = \sqrt{k}\psi_t, \tag{2.4.3.1a}$$

with

$$\mathcal{G}_t(\phi_t, \eta_t) = \frac{\mathrm{e}^{\mathrm{i}C_\pm}\sqrt{w}\mathrm{e}^{\mathrm{i}\pi/4}}{2\sqrt{2}(\delta - w)\sqrt{\pi}} \int_0^{\phi_t} \frac{\eta_t \Delta p^{(t)}(\xi)}{(\phi_t - \xi)^{3/2}} \mathrm{e}^{\mathrm{i}w\eta_t^2/2(\phi_t-\xi)} d\xi. \tag{2.4.3.1b}$$

We can use the solution from Tsai (1992) because it depends only on the pressure jump at the trailing edge rather than explicitly on the nature of the incident perturbation. Similarly, the transition solution for the camber dependence is similar to that presented in Myers and Kerschen (1997), subject to a rescaling in k, and a slight alteration of the phase to account for thickness dependence there. We take this solution in its final form

$$h_{ts}^{(c)} = \frac{\mathrm{e}^{\mathrm{i}kw\phi_t}}{\sqrt{k}} \left[J_{t0}(\phi_t, \eta_t) + \sqrt{k} \left(J_{t1,a}(\phi_t, \eta_t) + J_{t1,b}(\phi_t, \eta_t) \right) + O(\epsilon) \right], \tag{2.4.3.2}$$

where the $J_{ti,j}$ are given by

$$J_{t0} = \frac{-\mathrm{sgn}(\psi)\mathrm{e}^{\mathrm{i}C_\pm}}{2\sqrt{2+\phi_t}} \mathrm{e}^{\mathrm{i}w\eta_t^2/2(2+\phi_t)} \mathrm{e}^{\mathrm{i}kw\epsilon\sigma_1(0,0)} \left(P_l(0) \mathrm{e}^{\mathrm{i}k((w-\delta M_\infty^2)\Gamma/2+\epsilon w V(0)\int_0^2 q(r_t,0)dr)} \right.$$
$$\left. - P_l(2\pi) \mathrm{e}^{-\mathrm{i}k((w-\delta M_\infty^2)\Gamma/2+\epsilon w V(0)\int_0^2 q(r_t,2\pi)dr)} \right) \mathrm{erfc}\left[\frac{\mathrm{e}^{-\pi\mathrm{i}/4}\sqrt{w}|\eta_t|}{\sqrt{\phi_t(2+\phi_t)}} \right] \mathrm{e}^{\mathrm{i}k(w-\delta M_\infty^2)(2+\alpha_t)}, \tag{2.4.3.3}$$

$$J_{t1,a} = \mathrm{i}\epsilon w V(0) \eta J_{t0} \int_0^{\phi_t} \frac{\partial q_t^{(c)}}{\partial \psi_t}(\phi_t', 0) d\phi_t' - V(0)\epsilon \frac{\partial J_{t0}}{\partial \eta} \int_0^{\phi_t} \int_0^{\phi_t'} \frac{\partial q_t^{(c)}}{\partial \psi_t}(\phi_t'', 0) d\phi_t'', \tag{2.4.3.4}$$

and

$$J_{t1,b} = -\epsilon \frac{e^{iC_\pm} wV(0)i}{4\pi\beta_\infty} e^{ik(w-\delta M_\infty^2)(2+\alpha_t)+ikw\epsilon\sigma_1(0,0)} \left(P_l(0) e^{ik((w-\delta M_\infty^2)\Gamma/2+\epsilon wV(0)\int_0^2 q(r_t,0)dr)} \right.$$
$$\left. + P_l(2\pi) e^{-ik((w-\delta M_\infty^2)\Gamma/2+\epsilon wV(0)\int_0^2 q(r_t,2\pi)dr)} \right) \int_0^{\phi_t} \frac{\eta_t b_t(\nu) e^{iw\eta_t^2/2(\phi_t-\nu)}}{(\phi_t-\nu)^{3/2}} d\nu, \tag{2.4.3.5}$$

with

$$b_t(\phi_t) = \frac{2}{2+\phi_t} \int_0^2 \sqrt{2+\phi_t-\xi}\sqrt{\xi} y^{(c)\prime\prime}(\xi) d\xi. \tag{2.4.3.6}$$

Here, $J_{t1,a}(\phi_t, \eta_t)$ is the correction in the trailing-edge transition region that cancels the discontinuity in the vertical velocity across the wake (and has zero pressure jump) caused by the leading-edge camber-related field, and $J_{t1,b}(\phi_t, \eta_t)$ has continuous vertical velocity across the wake, but cancels the discontinuity in the pressure caused by the leading-edge camber-related field. For more details see Myers and Kerschen (1997).

2.4.4 Matching the Trailing-Edge Transition and Inner Solutions

Here we match the trailing-edge transition and inner solutions to ensure that our final region completes our solution for the acoustic field anywhere in the solution domain. We note first that when we expand $H_0^I(\theta_t)$ from (2.4.2.11) in terms of transition variables it becomes $O(k^{-1})$ and hence is negligible in the matching. Setting $\xi_1 = |\eta_t|/\sqrt{\phi_t - \xi}$ in (2.4.3.1b) as done by Tsai (1992) gives

$$G_t(\phi_t, \eta_t) = \frac{\mathrm{sgn}(\psi_t) e^{iC_\pm}\sqrt{w} e^{i\pi/4}}{\sqrt{2}(\delta-w)\sqrt{\pi}} \int_{|\eta_t|/\sqrt{\phi_t}}^{\infty} \Delta p^{(t)}(\phi_t - \eta_t^2/\xi_i^2) e^{iw\xi_1^2/2} d\xi_1. \tag{2.4.4.1}$$

We separate $\Delta p^{(t)}(\phi_t)$ into a term proportional to $\Delta p^{(t)}(0)$, and a correction of $O(tk^{-1/2})$. This is given explicitly in Appendix 2.10.

When we expand G_t in terms of the variables $\Phi_t = k\phi_t$ and $\rho_t = |\eta_t|/\sqrt{\phi_t} = |\Psi_t|/\sqrt{\Phi_t}$ we see immediately that the second term in $\Delta p^{(t)}$ vanishes to $O(\epsilon k^{-1/2})$, so

$$h_{ts}^{(t)} \sim \frac{\mathrm{sgn}(\psi_t) e^{ikw\sigma_t(\phi_t,0)}}{\sqrt{k}} \frac{e^{iC_\pm} i\Delta p^{(t)}(0)}{2(\delta-w)} \mathrm{erfc}\left(e^{-i\pi/4}\rho_t \frac{\sqrt{w}}{\sqrt{2}} \right). \tag{2.4.4.2a}$$

Writing (2.4.3.2) also in terms of these variables yields

$$h_{ts}^{(c)} \sim \frac{\mathrm{sgn}(\psi_t)\mathrm{e}^{\mathrm{i}kw\sigma_t(\phi_t,0)}}{\sqrt{k}} \frac{\mathrm{e}^{\mathrm{i}C_\pm}\mathrm{i}\Delta p^{(c)}(0)}{2(\delta - w)} \mathrm{erfc}\left(\mathrm{e}^{-\mathrm{i}\pi/4}\rho_t \frac{\sqrt{w}}{\sqrt{2}}\right). \tag{2.4.4.2b}$$

The contributions from J_{t1} are negligible during the matching process. Recall the inner solution, (2.4.2.7), and note that for the transition region we require the expansion of T that is uniformly valid for all θ_t, i.e. $T^u(\theta_t)$. Expanding this in terms of the transition region variables, η_t and ϕ_t, and taking the limit of large k we obtain

$$H_t \sim \frac{\mathrm{sgn}(\psi_t)\mathrm{i}\Delta p(0)\mathrm{e}^{\mathrm{i}C_\pm}}{2(\delta - w)\sqrt{k}} \mathrm{erfc}\left(\mathrm{e}^{-\mathrm{i}\pi/4}\frac{\sqrt{w\eta_t^2}}{\sqrt{2\phi_t}}\right) \mathrm{e}^{-\mathrm{i}w\eta_t^2/2\phi_t}\mathrm{e}^{\mathrm{i}kwr_t}, \tag{2.4.4.2c}$$

where we use the approximation $\theta_t \sim \eta_t/(\sqrt{k}\phi_t)$. Finally, we note that in the trailing-edge transition region $r_t \sim \phi_t + \eta_t^2/(2k\phi_t)$, hence we see that these two scattered solutions, h_{ts} and H_t, match since $\Delta p(0) = \Delta p^{(t)}(0) + \Delta p^{(c)}(0)$. We are not considering the h_{ls} term in the matching here because it is not a field scattered from the trailing edge, and has already matched its corresponding scattered field from the leading edge.

2.4.5 Far-Field Solution from the Trailing Edge

The outer trailing-edge solution is given by (2.4.1.5) and (2.4.2.14). Following the work of Myers and Kerschen (1997) and Tsai (1992), we expand this in terms of transition region variables, and expand the transition solution in terms of outer variables. When we write both in terms of transition region variables we see common terms for both camber and thickness. This ensures there is a matching between the trailing-edge transition and outer solutions, but we must subtract this common term from the total far-field solution to create a composite trailing-edge solution made up of the outer and transition solutions. The common term corresponding to the thickness parameter is

$$h_t^{(t)c} = -\frac{\mathrm{sgn}(\psi_t)\mathrm{e}^{\mathrm{i}\pi/4}\Delta p^{(t)}(0)\mathrm{e}^{\mathrm{i}C_\pm}\sqrt{\phi_t}}{\sqrt{2w\pi}|\eta_t|\sqrt{k}(\delta - w)} \mathrm{e}^{\mathrm{i}kw\phi_t + \mathrm{i}w\eta_t^2/2\phi_t + \mathrm{i}k\epsilon w\sigma_{t_1}(r_t,0)}, \tag{2.4.5.1a}$$

while for the camber parameters the common term is

$$h_t^{(c)c} = -\frac{\mathrm{sgn}(\psi_t)\mathrm{e}^{\pi\mathrm{i}/4}\mathrm{e}^{\mathrm{i}C_\pm}\sqrt{\phi_t}}{2\sqrt{\pi w}\sqrt{k}|\eta_t|} \mathrm{e}^{\mathrm{i}kw\phi_t + \mathrm{i}w\eta_t^2/2\phi_t} \left[1 + \frac{\mathrm{i}\sqrt{k}\eta_t\epsilon w V(0)}{\phi_t} \int_0^{\phi_t} \phi_t' \frac{\partial q^{(c)}}{\partial \psi_t}(\phi_t', 0) d\phi_t'\right]$$

$$\left(P_l(0)\mathrm{e}^{\mathrm{i}k((w-\delta M_\infty^2)\Gamma/2+\epsilon w V(0)\int_0^2 q(r,0)dr)} - P_l(2\pi)\mathrm{e}^{-\mathrm{i}k((w-\delta M_\infty^2)\Gamma/2+\epsilon w V(0)\int_0^2 q(r,2\pi)dr)}\right)$$
$$\mathrm{e}^{\mathrm{i}k(w-\delta M_\infty^2)(2+\alpha_t)+\mathrm{i}kw\epsilon\sigma_1^t(0,0)}. \quad (2.4.5.1b)$$

To obtain a uniformly-valid composite solution in the outer region of the trailing edge, denoted by h_t^u, we must subtract this common term, therefore giving

$$h_t^u = h_t + h_{ts} - h_t^c. \quad (2.4.5.2)$$

We did not have to subtract a common term when considering the leading-edge transition solution because the leading-edge transition solution had a negligible effect in the far field (except at $O(\sqrt{k})$ angles from $\theta = 0$ which we corrected with the trailing-edge transition solution).

The final expression for total far-field trailing-edge acoustic potential is given by

$$h_t^u(r_t,\theta_t) \sim \frac{\mathrm{e}^{\mathrm{i}C_\pm}\mathrm{e}^{\mathrm{i}kw\sigma_t(r_t,\theta_t)}}{\sqrt{2}k\sqrt{r_t}(\delta - w\cos\theta)}\left\{-\mathrm{sgn}(\psi_t)\mathrm{i}\mathrm{e}^{-2\mathrm{i}kw(1-\cos\theta_t)}(P_+ - P_-)\right.$$
$$\mathrm{erfc}\left[\mathrm{e}^{-\pi\mathrm{i}/4}\sqrt{2kw(1-\cos\theta)}\right] - \frac{2\sqrt{kw}V(0)(\alpha_i - \epsilon y^{(c)\prime}(2))(P_+ - P_-)\mathrm{e}^{\pi\mathrm{i}/4}}{\sqrt{\pi}\beta_\infty}$$
$$\left(1 - \sqrt{2kw\pi(1-\cos\theta)}\mathrm{e}^{-2\mathrm{i}kw(1-\cos\theta)-\pi\mathrm{i}/4}\mathrm{erfc}\left[\mathrm{e}^{-\pi\mathrm{i}/4}\sqrt{2kw(1-\cos\theta)}\right]\right)$$
$$\left. + \frac{\mathrm{sgn}(\psi_t)\epsilon\sqrt{kw}V(0)(P_+ + P_-)}{\sqrt{2}\pi\beta_\infty}\sqrt{kw(1-\cos\theta)}\int_0^\infty \mathrm{e}^{\mathrm{i}kw(1-\cos\theta)\xi}b_t(\xi)d\xi\right\}$$
$$+ \frac{\mathrm{sgn}(\psi)\mathrm{e}^{\mathrm{i}C_\pm}\mathrm{e}^{\mathrm{i}kw\sigma_t(r_t,\theta_t)}}{k\sqrt{r_t}(\delta - w)}\left\{\frac{\Delta p^{(t)}(0)\mathrm{e}^{\pi\mathrm{i}/4}|\sin\theta_t/2|}{\sqrt{2\pi w}(\delta - w\cos\theta)}\right.$$
$$+ \frac{\Delta p^{(t)}(0)}{\sqrt{2}}\mathrm{i}\sqrt{k}\mathrm{e}^{-2\mathrm{i}kw(1-\cos\theta_t)}\mathrm{erfc}\left[\mathrm{e}^{-\pi\mathrm{i}/4}\sqrt{2kw(1-\cos\theta)}\right]$$
$$+ \frac{tk\mathrm{i}\beta_\infty\sin\chi\mathrm{e}^{\pi\mathrm{i}/4}\sqrt{w}(\delta - w)}{2\pi^{3/2}\sqrt{\cos\chi+1}(\cos\chi-1)}\left(1 - \frac{(\gamma+1)M_\infty^4}{2\beta_\infty^4 w^2}(\delta - w)^2\right)\mathrm{e}^{\mathrm{i}k(w-\delta M_\infty^2)(2+\alpha_t)+\mathrm{i}kw\epsilon\sigma_1(0,0)}$$
$$\left[\mathrm{e}^{\mathrm{i}k(w-\delta M_\infty^2)\Gamma/2+\mathrm{i}kw\epsilon\sigma_{l_1}(2,0)}\left\{\mathrm{e}^{\pi\mathrm{i}/4}\frac{\sqrt{\pi}}{\sqrt{2w}}\int_0^2\left(\frac{a}{\tau} + \frac{\beta_\infty}{t'\tau^{3/2}}\int_0^\tau \frac{\partial q^{(t)}}{\partial\theta}(r,0)dr\right)\right.\right.$$
$$\mathrm{e}^{\mathrm{i}kw(1-\cos\theta)\tau}\mathrm{erfc}\left[\mathrm{e}^{-\pi\mathrm{i}/4}\sqrt{2-\tau}\sqrt{kw(1-\cos\theta)}\right]d\tau + 2a\sqrt{k(1-\cos\theta)}$$
$$\int_2^\infty \mathrm{e}^{\mathrm{i}kw(1-\cos\theta)\xi^2/2}\left[\log[2] - \log[\xi^2/2] - \log[1-\sqrt{1-4/\xi^2}]\right]d\xi$$
$$+ \frac{\beta_\infty}{t'}\int_0^2 \frac{\partial q^{(t)}}{\partial\theta}(r,0)dr\sqrt{2k(1-\cos\theta)}\int_2^\infty \sqrt{1-4/\xi^2}\mathrm{e}^{\mathrm{i}kw(1-\cos\theta)\xi^2/2}d\xi -$$
$$\left.\left.\frac{\sqrt{\pi}}{\sqrt{w}}\mathrm{erfc}\left[\mathrm{e}^{-\pi\mathrm{i}/4}\sqrt{2kw(1-\cos\theta)}\right]\int_0^2\left(\frac{a}{\tau} + \frac{\beta_\infty}{t'\tau^{3/2}}\int_0^\tau \frac{\partial q^{(t)}}{\partial\theta}(r,0)dr\right)\frac{d\tau}{\sqrt{2-\tau}}\right\}\right.$$
$$\left. + \mathrm{e}^{-\mathrm{i}k(w-\delta M_\infty^2)\Gamma/2+\mathrm{i}kw\epsilon\sigma_{l_1}(2,2\pi)}\left\{\mathrm{e}^{\pi\mathrm{i}/4}\frac{\sqrt{\pi}}{\sqrt{2w}}\int_0^2\left(\frac{a}{\tau} + \frac{\beta_\infty}{t'\tau^{3/2}}\int_0^\tau \frac{\partial q^{(t)}}{\partial\theta}(r,2\pi)dr\right)\right.\right.$$

$$\mathrm{e}^{\mathrm{i}kw(1-\cos\theta)\tau}\mathrm{erfc}\left[\mathrm{e}^{-\pi\mathrm{i}/4}\sqrt{2-\tau}\sqrt{kw(1-\cos\theta)}\right]d\tau+2a\sqrt{k(1-\cos\theta)}$$
$$\int_2^\infty \mathrm{e}^{\mathrm{i}kw(1-\cos\theta)\xi^2/2}\left[\log[2]-\log[\xi^2/2]-\log[1-\sqrt{1-4/\xi^2}]\right]d\xi$$
$$+\frac{\beta_\infty}{t'}\int_0^2\frac{\partial q^{(t)}}{\partial\theta}(r,2\pi)dr\sqrt{2k(1-\cos\theta)}\int_2^\infty\sqrt{1-4/\xi^2}\mathrm{e}^{\mathrm{i}kw(1-\cos\theta)\xi^2/2}d\xi-$$
$$\frac{\sqrt{\pi}}{\sqrt{w}}\mathrm{erfc}\left[\mathrm{e}^{-\pi\mathrm{i}/4}\sqrt{2kw(1-\cos\theta)}\right]\int_0^2\left(\frac{a}{\tau}+\frac{\beta_\infty}{t'\tau^{3/2}}\int_0^\tau\frac{\partial q^{(t)}}{\partial\theta}(r,2\pi)dr\right)\frac{d\tau}{\sqrt{2-\tau}}\Bigg\}\Bigg]$$
$$+\frac{\mathrm{i}\sin\chi\mathrm{e}^{-\mathrm{i}\beta_t^2}(\delta-w)k\sqrt{r_t}}{2\sqrt{1-\cos\chi}\sqrt{1+\cos\theta_t}}\mathrm{sgn}(\beta_t)\mathrm{erfc}\left[\mathrm{e}^{-\pi\mathrm{i}/4}|\beta_t|\right]\mathrm{e}^{\mathrm{i}k(w\cos\chi-\delta M_\infty^2)(2\pm\Gamma/2+\alpha_t)}\mathrm{e}^{\mathrm{i}kw\epsilon\sigma_1^t(0,0)}\Bigg\},\tag{2.4.5.3}$$

where

$$P_\pm=\frac{\mathrm{i}}{\sqrt{2}}(w-\delta)P_l(0\pm)\mathrm{e}^{\pm\mathrm{i}k((w-\delta M_\infty^2)\Gamma/2+w\epsilon V(0)\int_0^2 q(r,0\pm)dr)+\mathrm{i}k(w-\delta M_\infty^2)(2+\alpha_t)+\mathrm{i}kw\epsilon\sigma_1(0,0)}\tag{2.4.5.4}$$

and the camber-dependent pressure jump at the trailing edge is given by $P_+ - P_-$.

2.5 Total Far-Field Solution

At this point we briefly summarise our analysis. The total far-field scattered pressure directivity is dominated by direct scattering from the leading and trailing edges, and in addition more sound is generated by the interaction of the incident sound wave with the aerofoil and the locally non-uniform mean flow in the leading-edge region (Sect. 2.2). In the outer region the length scale of the mean-flow gradients scales with the chord length of the aerofoil, and the distortion of the sound wave is sufficiently slow that no additional sound is generated in this region. However, sound propagates away from the leading- and trailing-edge regions through the outer region, and undergoes a refractive phase shift of $O(1)$ (Sect. 2.3.1). There are transition regions above and below the aerofoil which account for the surface curvature, and are seen as rays propagating from the leading edge along the upper and lower surfaces of the aerofoil (Sect. 2.3.2). These rays are then scattered by the trailing edge (Sects. 2.4.1 and 2.4.2). The trailing-edge transition solution cancels the discontinuous pressure across the wake caused by the leading-edge ray fields above and below the aerofoil (Sect. 2.4.3). A further contribution to the outer solution is h^o from (2.3.0.1), which arises from the incident sound wave being directly reflected or blocked by the aerofoil surface. In the far-field this only has an effect in a small $O(1/r)$ region at $\theta=\chi$, and at distances of $r=O(k)$ from the aerofoil this direct field is overpowered by the scattered Fresnel fields in a similar manner to that discussed in Peake and Kerschen (2004), therefore we do not consider its effects from now on and instead discuss just the scattered solution.

We have obtained solutions for the leading- and trailing-edge ray fields, h_l^u and h_t^u. To obtain a uniformly-valid expansion, we replace any non-uniform terms with their uniformly-valid counterparts, as explained in Sect. 2.3.1. We add the two fields to find the total acoustic far-field potential,

$$h = h_l^u + h_t^u,$$

which can be written as

$$h = \mathrm{e}^{\mathrm{i}kw\sigma_l}\left[D_l^u(r,\theta) - D_t^u(r,\theta)\mathrm{e}^{\mathrm{i}kw\sigma_s}\right], \tag{2.5.0.1}$$

where σ_s is the phase shift between the leading- and trailing-edge ray fields, as measured by an observer in the far field at angle θ from the leading edge. The functions, $D_{l,t}^u(r,\theta)$, are the uniformly-valid contributions to the total pressure from the leading and trailing edge respectively. We choose a negative sign between the leading- and trailing-edge fields so that the real parts of the Fresnel region contributions both have the same sign.

In the far field, the phase shift, σ_s, is given by

$$\begin{aligned}\sigma_s^{\pm} &= \sigma_t - \sigma_l \\ &= \frac{V(\theta)}{\beta_\infty}\left(2\alpha_i \sin\theta + \cos\theta(\pm\alpha_g\pi + \beta_\infty\alpha_t)\right) \\ &\quad + \left(2 \pm \frac{\alpha_g\pi}{\beta_\infty} + \alpha_t\right)\cos\theta - \mathrm{i}kw\epsilon\sigma_1(0,0),\end{aligned} \tag{2.5.0.2}$$

and α_g is as defined in (2.4.1.3). The "$\pm$" denotes the phase shift above and below the aerofoil respectively, and is present due to the non-zero mean circulation. The first term in (2.5.0.2) corresponds to the different refraction experienced by the sound emanating from the leading- and trailing-edge sources en-route to an observer above or below the aerofoil, whilst the second term arises simply from the fact that the leading and trailing edges are located at different positions in (ϕ, ψ) space. The final term is due to the distortion of the incident sound wave as it approaches the leading edge, and is a constant. The term α_g is crucial in explaining why the acoustic pressures above and below the aerofoil differ as we alter the camber, thickness and angle of attack. We return to this in the next section.

2.6 Results and Discussion

2.6.1 Far-Field Pressure Directivity for the Scattered Sound

Here we present results for the far-field scattered pressure directivity (i.e. not including the incident wave), as determined from our analytic solutions h_l^u and h_t^u. The

pressure directivity is plotted in physical space, and polar coordinates (r_p, θ_p) in physical space are related to (r, θ) in potential-streamfunction space via

$$r = (1 - M_\infty^2 \sin\theta)^{1/2} r_p + O(t, \alpha_{\text{eff}}), \tag{2.6.1.1a}$$

$$\cos\theta = \frac{\beta_\infty \cos\theta_p}{\sqrt{1 - M_\infty^2 \cos^2\theta_p}}. \tag{2.6.1.1b}$$

The $O(t, \alpha_{\text{eff}})$ term in (2.6.1.1) provides only a phase shift to the total solution in the factor $\mathrm{e}^{\mathrm{i}kw\sigma_l}$ from (2.5.0.1), and hence does not affect the amplitude of the pressure directivity (Myers and Kerschen 1997). Our uniformly-valid composite expansions are plotted for r_p greater than the Rayleigh distance, $O(k)$, to ensure that the acoustic far-field behaviour is captured correctly (i.e. the Fresnel regions from the leading and trailing edges have overlapped). In what follows, we omit the subscripted p and refer only to physical space coordinates, and set $k_3 = 0$ in (2.1.2.4b).

We explicitly consider the NACA 4-digit series of aerofoils to illustrate our results as these are well known and widely used in industry (Abbott and Von Doenhoff 1959). The surfaces of such aerofoils are given by the non-dimensionalised functions

$$y_\pm = Y^{(c)} \pm y^{(t)} \cos\varphi, \qquad x_\pm = x \pm y^{(t)} \sin\varphi, \tag{2.6.1.2a}$$

where $\pm$ denotes the upper and lower surfaces of the aerofoil respectively, and (x, y) are Cartesian coordinates with origin at the aerofoil leading edge. We define $Y^{(c)}(x)$, $y^{(t)}(x)$ and $\varphi(x)$ by

$$Y^{(c)} = -\alpha_i' x + y^{(c)}(x), \tag{2.6.1.2b}$$

$$\epsilon y^{(c)} = \begin{cases} \frac{mx}{p^2}(2p - \frac{x}{2}) & 0 \le x \le 2p \\ \frac{m(2-x)}{(1-p)^2}(1 + \frac{x}{2} - 2p) & 2p \le x \le 2 \end{cases}, \tag{2.6.1.2c}$$

$$y^{(t)} = \frac{2t'}{0.2}\left(a_1\sqrt{\frac{x}{2}} - a_2\frac{x}{2} - a_3\frac{x^2}{2^2} + a_4\frac{x^3}{2^3} - a_5\frac{x^4}{2^4}\right), \tag{2.6.1.2d}$$

$$\varphi(x) = \arctan\left[\frac{dy^{(c)}}{dx} + \alpha_i\right], \tag{2.6.1.2e}$$

with

$$a_1 = 0.2969, \quad a_2 = 0.1260, \quad a_3 = 0.3516, \quad a_4 = 0.2843, \quad a_5 = 0.1036. \tag{2.6.1.2f}$$

The standard choice of a_5 is 0.1015 (Abbott and Von Doenhoff 1959), however our choice of a_5 sets the position of the trailing edge to be $(2, 0)$ which proves more convenient for computation. Analytically this small alteration is negligible to

the orders retained during calculations. The superscripts c and t denote camber and thickness respectively, while the term $-\alpha_i x$ in (2.6.1.2) corresponds to the aerofoil being at the angle of attack $\alpha_i = \epsilon\alpha_i'$. Here, 2 is the chord length, $0 \leq x \leq 2$ is the position along the chord, ϵy is the half thickness at a given value of x from the centreline to the surface, $t = \epsilon t'$ is the maximum thickness as a fraction of the chord length, m is the maximum camber as a fraction of the chord length, and p is the location of the maximum camber along the centreline as a fraction of the chord length. A NACA 4-digit series aerofoil is defined entirely by the choice of p,m and t: 100m gives the first digit, 10p gives the second digit and 100t gives the last two digits.

Figure 2.6 shows the effect of changing the freestream Mach number, M_∞. An increase in Mach number increases the acoustic pressure amplitude everywhere around the aerofoil, and increases the modulation in the upstream direction (the left-half plane), i.e. a larger Mach number produces more lobes in the upstream direction. This effect arises from the relationship between w and M_∞ (see (2.1.2.4b)); as M_∞ increases, so too does w, causing a more rapid phase variation. There is an extra modulation of the phase above the aerofoil when compared to below, due to the phase shift between the leading and trailing edges; particularly the term depending on mean loading parameter $\alpha_g V(\theta)$. As analysed in Myers and Kerschen (1997), this adds to the phase variation in the upper half plane, but subtracts from it in the lower half

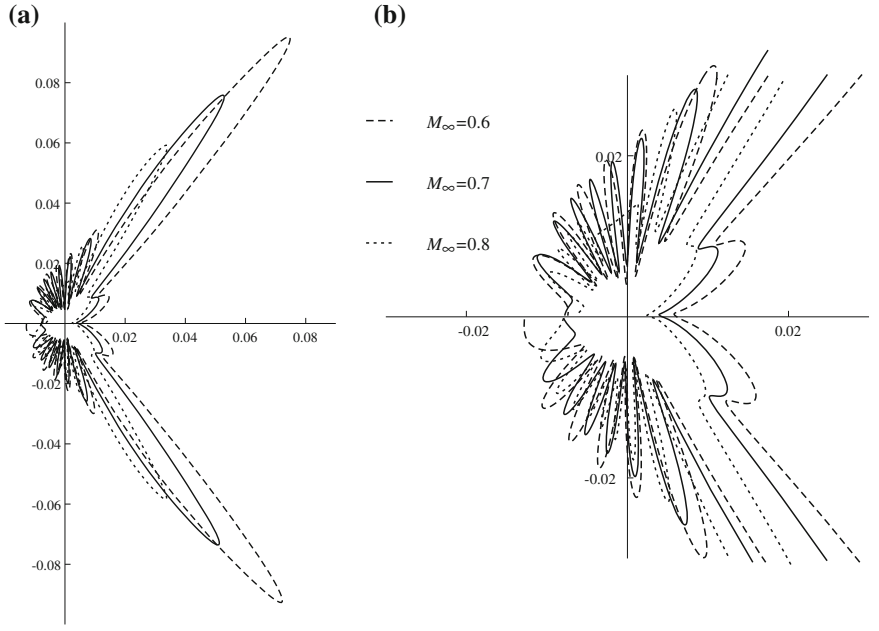

Fig. 2.6 Far-field scattered pressure directivity for a NACA 1112 aerofoil, $k = 6$, $\alpha_i = 0°$, $\chi = 45°$, $kw = 10$. The Mach number is varied from 0.6 to 0.8. **a** Full range. **b** Centre detail

plane, due to the sign of the perturbation flow velocity ϵq; a positive q (i.e. above the aerofoil) gives a larger speed of the surrounding flow in the downstream direction, whereas a negative sign decreases the speed, hence reducing the modulation. We see that the pressure directivity in the Fresnel regions (the large lobes above and below the aerofoil) is finite thanks to our uniformly-valid solution; this is a feature of all results given here.

The effect of varying aerofoil thickness is shown in Fig. 2.7. As we increase thickness, we decrease the magnitude of the pressure levels directly upstream (the negative real axis). This is a result of the slowing of the steady flow as it approaches a thick body. The pressure in the Fresnel regions increases in magnitude, due to multiplicative factors of $t\sqrt{k}$ appearing in the corrections to the pressure amplitude that come from (2.2.0.3). This effect is caused by additional Fresnel contributions being produced for a thick aerofoil hence we see increased reflection or shadow contributions.

Figure 2.8 shows the effect of varying the angle of attack of a NACA 1112 aerofoil. There is little amplification in the overall magnitude of the radiation (excluding in the Fresnel regions), due to the increase in α_{eff} being only small when we increase the angle of attack α_i. Recall the significance of α_{eff} is that in the inner leading-edge region the camber-dependent part of ϵq scales multiplicatively with α_{eff}, thereby inducing the effect of both the angle of attack of the mean chord line and the camber relative to the mean chord line. The modulation is increased above the aerofoil

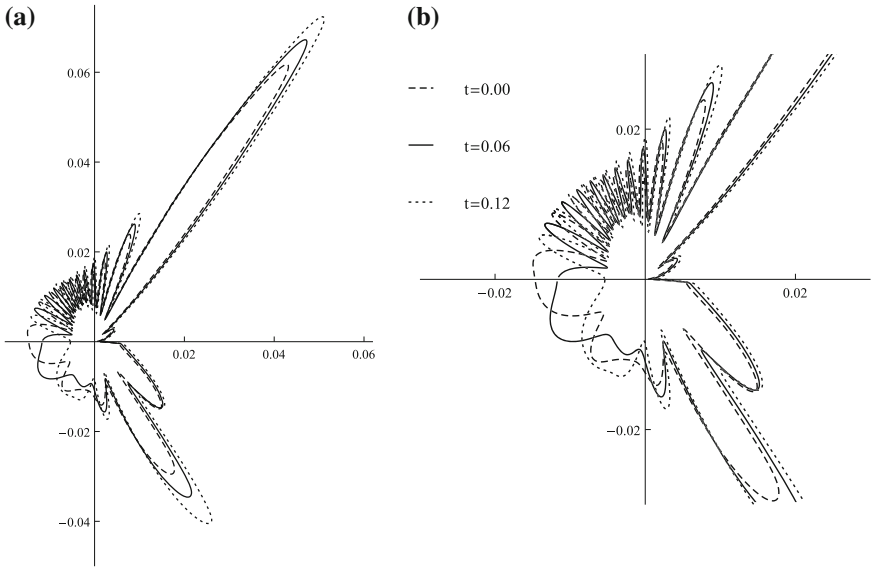

Fig. 2.7 Far-field scattered pressure directivity for a NACA 4-digit aerofoil with 10 % maximum camber at 10 % chord length, $k = 6$, $\alpha_i = 0°$, $\chi = 45°$, $kw = 10$, $M_\infty = 0.7$. The thickness ratio is varied from 0 to 12 %. **a** Full range. **b** Centre detail

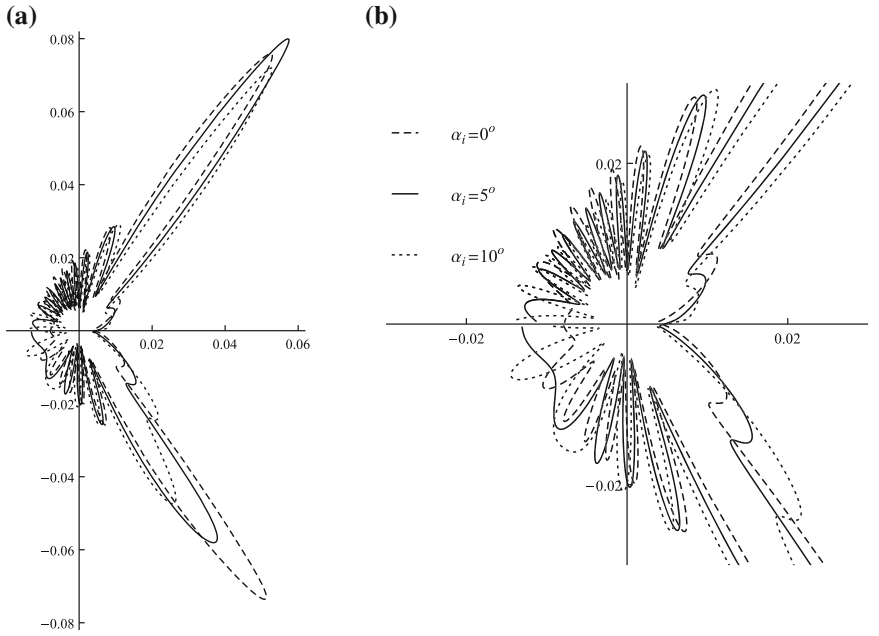

Fig. 2.8 Far-field scattered pressure directivity for a NACA 1112 aerofoil with $k = 6$, $\chi = 45°$, $kw = 10$, $M_\infty = 0.7$. The angle of attack is varied from 0° to 10°. **a** Full range. **b** Centre detail

for greater incidence angle, for similar reasons to those discussed for increasing Mach number in Fig. 2.6. The pressure amplitude in the Fresnel regions varies in an apparently complicated way with varying α_i, and this is caused by variations in magnitude of the directivity function, along with the phase shift between the leading and trailing Fresnel expansions being different above and below the aerofoil, which is discussed in more detail later.

Figure 2.9 shows the effect of varying χ, the angle of propagation of the incident sound wave. Clearly as we alter χ the shadow and reflection boundaries move, and hence the directions of the Fresnel regions (which lie on these boundaries) also move. We also notice that there is an increase in the magnitude of the sound pressure level as we increase χ. This is caused by the fact that the amplitude of the flat-plate solution, (2.2.1.9), scales as $\sin(\chi/2)$, corresponding to the increase in the blocking of unsteady momentum by the aerofoil as the sound wave is rotated closer to the normal direction. Figure 2.10 shows the effect of varying kw. Physically this corresponds to varying the frequency of the incident sound wave. In the upstream direction, the pressure directivity increases in magnitude as kw increases, since w is a multiplicative factor of the pressure (recall, the pressure can be obtained from the modified potential h via (2.1.2.5)). We have found that the flat-plate solution has $h \sim (kw)^{-1/2} e^{ikwr}$, hence the flat-plate pressure contribution has a multiplicative factor of $w^{1/2}$). The other

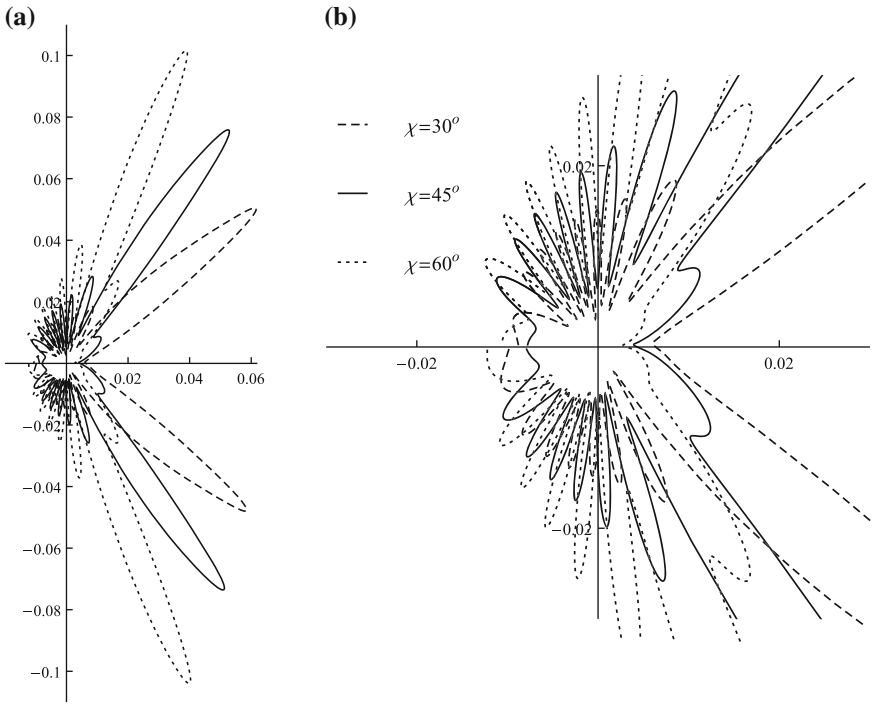

Fig. 2.9 Far-field scattered pressure directivity for a NACA 1112 aerofoil with $k = 6$, $\alpha_i = 0°$, $kw = 10$, $M_\infty = 0.7$. The angle of the incident sound wave, χ, is varied from 30° to 60°. **a** Full range. **b** Centre detail

effect of increasing kw is simply to increase the modulation everywhere around the aerofoil (due to kw being the scaling of all phase terms in the far-field sound).

Finally, Fig. 2.11 shows the effect of varying the percentage of maximum camber of the aerofoil for an incident sound wave emanating from far downstream i.e. from the bottom right of Fig. 2.1. The modulation of the far-field pressure directivity is due to the interference of the leading- and trailing-edge fields, and as can be seen in the previous results is strongest in the upstream direction. This time, however, the Fresnel regions are directed upstream and thereby envelope much of the modulation, so that the directivity in Fig. 2.11 is less oscillatory than for sound incident from upstream. The upper leading-edge Fresnel zone is visibly modulated however, and this modulation increases with increasing camber; this is for identical reasons as to the increasing modulation found in Figs. 2.6, 2.7 and 2.8. We also see here another example of a complicated variation in the magnitude of the pressure with varying aerofoil geometry in the Fresnel regions, similar to Fig. 2.8.

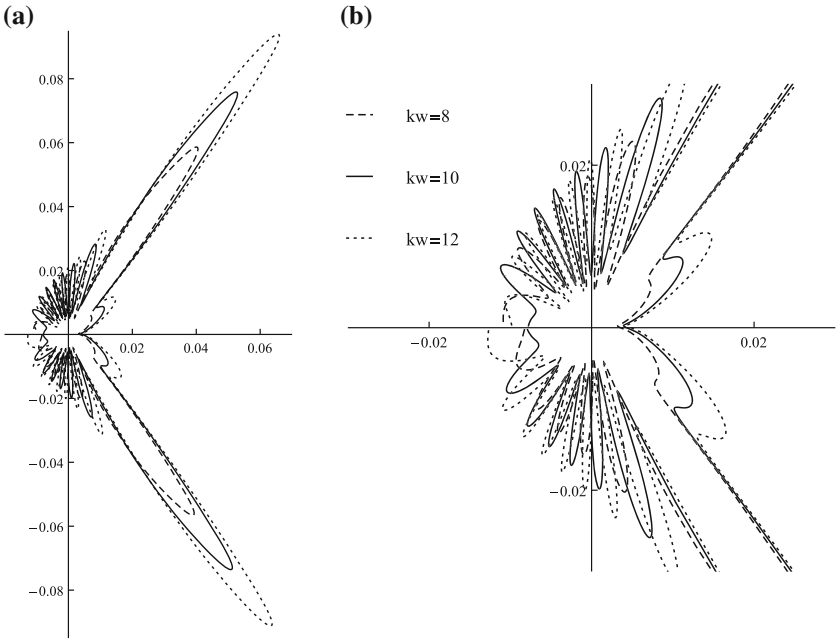

Fig. 2.10 Far-field scattered pressure directivity for a NACA 1112 aerofoil with $k = 6$, $\alpha_i = 0°$, $\chi = 45°$, $M_\infty = 0.7$. The acoustic frequency, kw, is varied from 8 to 12. **a** Full range. **b** Centre detail

2.6.2 Total Far-Field Pressure

In what follows we set $M_\infty = 0.7$, $kw = 10$ and $\chi = 45°$, and investigate the maximum and minimum total scattered far-field pressure, by summing the incident pressure and the scattered pressure, and normalizing by the incident pressure. The maximum and minimum pressures occur within the reflection and shadow Fresnel regions, respectively. Each maximum and minimum is generated by two Fresnel regions combining in the far field, emanating from the leading and trailing edges of the aerofoil, which have a phase shift between them. This phase shift, σ_s in (2.5.0.2), is an important factor in determining the nature of the total pressure within the Fresnel regions, and depends strongly on the non-uniform mean flow around the aerofoil.

To illustrate the importance of the phase shift, consider Fig. 2.12 and Table 2.1; for 0 % thickness at $\alpha_i = -5°$, the Fresnel region contributions are almost in and out of phase above and below the flat plate respectively, with the phase shift above the plate being close to 0, and the shift below being close to π. Hence above the plate, we subtract the magnitude of the scattered field generated at the trailing edge from the scattered field generated at the leading edge (we subtract when the fields are in phase because there is an overall negative sign difference between the relevant contributions in the leading- and trailing-edge fields in (2.5.0.1)). Below the plate,

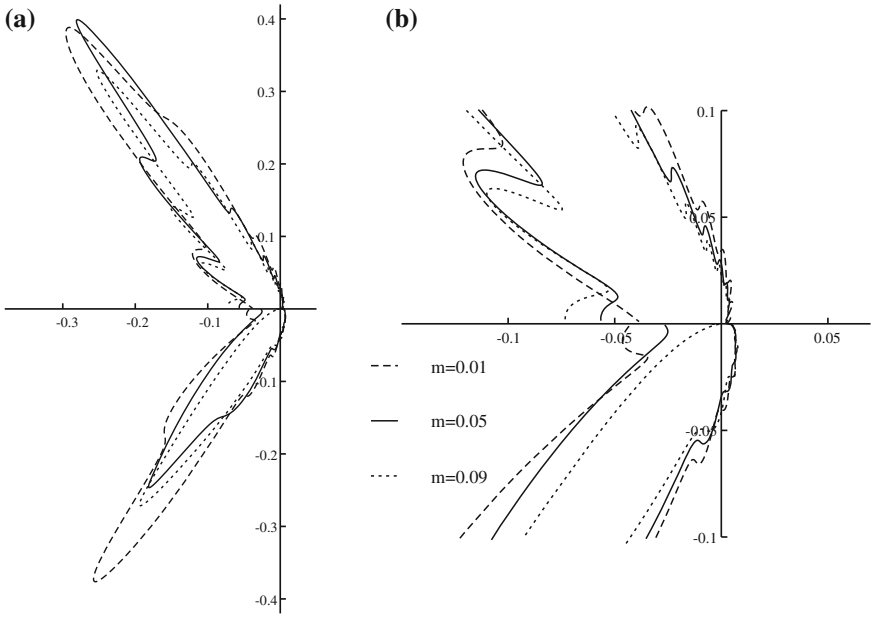

Fig. 2.11 Far-field scattered pressure directivity for a NACA 4-digit aerofoil with maximum camber at 10 % chord length, and 12 % thickness, $k = 6$, $kw = 10$, $\alpha_i = 0°$, $\chi = 135°$, $M_\infty = 0.7$. The percentage of maximum camber is varied from 1 to 9 %. **a** Centre detail. **b** Full range

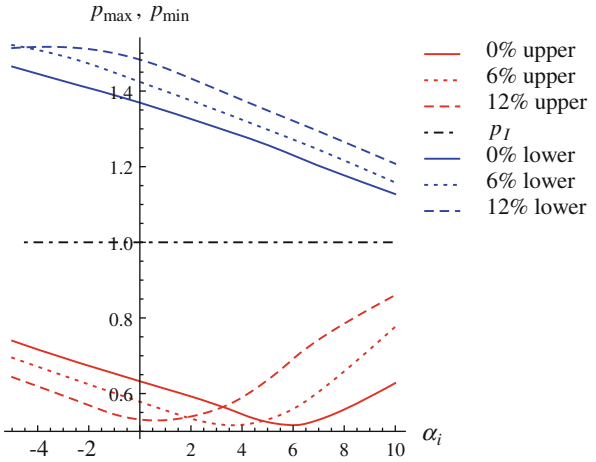

Fig. 2.12 Maximum and minimum total far-field pressure (normalised with respect to the incident pressure), as functions of angle of attack, for uncambered NACA 4-digit aerofoils. The legend denotes maximum thickness in % of chord length and the location; either in the upper (shadow) or lower (reflection) Fresnel region. p_I denotes the pressure generated by the incident sound wave

Table 2.1 Values of the phase shift above and below the flat-plate aerofoil modulo 2π

α_i (°)	$kw\sigma_s^+$	$kw\sigma_s^-$	$kw(\sigma_s^+ - \sigma_s^-)$
−5	0.46	2.69	−2.23
−3	0.91	2.25	−1.34
0	1.58	1.58	0.00
3	2.25	0.91	1.34
5	2.69	0.46	2.23
7	3.14	0.01	3.13
10	−2.47	−0.66	−1.81

because the fields are almost out of phase, we end up summing their magnitudes. Thus the upper solid curve (denoting the maximum pressure below the plate) in Fig. 2.12 is further from the (unit) amplitude of the incident pressure than the lower solid curve (denoting the minimum pressure above the plate).

As we increase the angle of attack, the phase shift above the plate increases, whilst the phase shift below the plate decreases, and the overall phase shift difference comes closer to 0, and equals zero at zero angle of attack. In this case, the flat plate is aligned with the steady mean flow, hence we expect that, for any angle of propagation of incident sound wave, the pressure perturbation above the plate mirrors that below the plate. This is precisely the case seen in Fig. 2.12 where for any value of thickness, at $\alpha_i = 0$ the maximum and minimum total pressures are equidistant from unit pressure. As we increase the angle of attack further still, the phase shift above the plate still increases and the phase shift below the plate still decreases, and as these values approach π and 0, we begin adding and subtracting the magnitudes of the pressure from the leading-edge scattered field and the trailing-edge scattered field respectively, which results in the upper curve approaching unit pressure, and the lower curve tending further from unit pressure. This process occurs until $\alpha_i \approx 7°$ at which point both the maximum and minimum pressure curves approach minimum values (for larger values of α_i, we begin to veer out of the $\alpha_i = O(\epsilon)$ region so the results are less reliable). One anticipates the maximum and minimum pressures will continue to oscillate as we increase the angle of attack, and the troughs of the maximum and minimum pressure curves will occur when the pressure shift difference between them are close to π, whereas the peaks will occur when the difference is close to $-\pi$.

The variation of maximum and minimum pressure for a cambered aerofoil is shown in Fig. 2.13. There is symmetry about unit pressure for zero camber for all values of thickness plotted here, because once again the phase shifts between the leading and trailing Fresnel regions are the same above and below the aerofoil, for zero camber. Upon varying the amount of camber, we not only vary the phase shift between the Fresnel regions, we also alter the shape of the leading and trailing edges with respect to the incident flow, and hence get a variation in magnitude of the leading- and trailing-edge scattered pressure fields as well as the variation in phase.

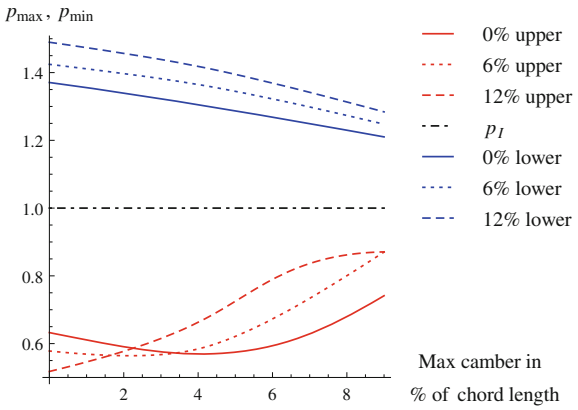

Fig. 2.13 Maximum and minimum total far-field pressure (normalised with respect to the incident pressure), as functions of maximum percentage camber, for NACA 4-digit aerofoils with maximum camber at 10 % chord and zero angle of attack. The legend denotes maximum thickness in % of chord length and the location; either in the upper (shadow) or lower (reflection) Fresnel region. p_I denotes the pressure generated by the incident sound wave

Thus there is little symmetry anywhere else in any of the curves in this figure, but it illustrates the complicated nature of the sound scattered in the Fresnel regions as we alter the aerofoil geometry.

2.7 Conclusions

This chapter has investigated the scattering of a high-frequency sound wave by an aerofoil in steady mean flow. In particular, a uniformly-valid far-field solution for the scattered acoustic pressure has been found, correct to the leading two terms in both the amplitude and the phase. In the high-frequency limit the far-field sound is dominated by scattering from the leading and trailing edges, and the magnitude of the scattered pressure is greatest in the Fresnel reflection and shadow regions. The existence of these Fresnel regions represents a structural difference between our results and the work of (Myers and Kerschen 1995, 1997) and Tsai (1992), who considered an incident gust rather than an incident sound wave. A number of physical insights have arisen from our analysis; first, the difference in refraction experienced by the sound from the leading and trailing edges en-route to the observer, represented by the quantities $\sigma_s^{\pm}$, plays a key role. For instance (in Figs. 2.6 and 2.7) the aerofoil camber and mean loading have a direct effect on the number of lobes in the sound field, while (in Figs. 2.12 and 2.13) refraction is shown to have a significant effect on the amplitudes in the Fresnel regions (i.e. on the amplitude of the total reflected field and on the depth of the shadow). Secondly, the aerofoil geometry and non-uniform

flow close to the leading edge can have an appreciable effect, especially in the Fresnel region (see Fig. 2.7, where we vary the thickness with everything else held fixed).

We have also seen that the angle of incidence plays an important role; the sound pressure level of the scattered field increases with sound incidence angle (Fig. 2.9), which is seen to be due in part to the increased momentum blocking for oblique sound waves. Further, the character of the sound field changes between cases in which the incident sound comes from upstream and from downstream, which is seen to be due to the Fresnel regions dominating the highly oscillatory diffracted field upstream in the latter case (Fig. 2.11). The precise implications of this effect for rotor blockage will only become clear once a cascade calculation has been completed, but given that the cascade noise is highly sensitive to the interference of the scattered field from different blades, we can speculate that the possible constructive interference of the upstream Fresnel regions of the different blades could reduce the opacity of a rotor to sound generated downstream.

The results in this chapter are applicable to any aerofoil with a parabolic leading edge, with nose radius scaling with thickness squared, and a sharp trailing edge, although aerofoils with different leading-edge shapes can be analysed using the same steps laid out by this chapter. The parabolic leading edge is convenient for both industrial aerofoils such as the NACA series, and mathematical aerofoils such as the Joukowski aerofoil.

Whilst new sound power is not created during the interaction of the incident field with the aerofoil, it is scattered and redirected by the aerofoil, and understanding this process is of great importance if one wishes to optimise shielding within an aeroengine. A principal benefit of the work presented here is in Sect. 2.6.2; this analysis allows the location and magnitude of the maximum total pressure obtained during sound-aerofoil interaction to be calculated swiftly and easily. Moreover this maximum can be calculated for a variety of aerofoil geometries and flow conditions with little difficulty, hence optimal aerofoil geometries can quickly be specified. Compare this method to computationally calculating the far-field pressure for many aerofoils (just one such calculation takes a substantial amount of time and processing power), and it becomes clear how this work could be useful to industry. Furthermore, as mentioned in the introduction to this dissertation, current computational schemes only run in low- to mid-range frequencies; high-frequency results are increasingly hard to compute.

It must be noted that the effects of a turbulent boundary layer have been neglected, and it is well-known that the interaction of turbulence with the trailing edge is a very important additional source of sounds (Ffowcs Williams and Hawkings 1969; Howe 1978). Furthermore there is an upper limit of validity of the Kutta condition we apply at the trailing edge, namely $k < O(Re^{1/4})$, with Re the Reynolds number based on chord length. A detailed discussion of this limit can be found in Crighton (1985). A further and more obvious breakdown of our analysis occurs when the angle of attack approaches the stall angle. For thin aerofoils this restricts the applications of our theory to aerofoils at small angles of attack, but for cascades this restriction is not so severe, given the flow turning induced upstream.

Appendices

2.8 Leading-Edge Inner Solution H_{3p}

Upon substituting the solution for H_0, (2.2.1.3), into the right hand side of (2.2.4.1a) and by using the same method as Tsai (1992)[1] we find the particular solution of (2.2.4.1a), denoted with a hat, to be

$$\begin{aligned}\hat{H}_{3p} =& \frac{\mathrm{i}\sqrt{w}\sin\chi\,\beta_\infty\tilde{a}}{\pi\sqrt{\cos\chi+1}}\left(\sqrt{R}\cos\frac{\theta}{2}\int_{-\infty}^{\infty}\frac{\sqrt{\lambda-w}\mathrm{e}^{a(\lambda,R,\theta)}}{\lambda+w\cos\chi}\left[1-\frac{(\lambda+\delta)^2(\gamma+1)M_\infty^4}{2\beta_\infty^4 w^2}\right]d\lambda\right.\\ &\left.-\mathrm{isgn}(\Psi)\sqrt{R}\sin\frac{\theta}{2}\int_{-\infty}^{\infty}\frac{\lambda\mathrm{e}^{a(\lambda,R,\theta)}}{\sqrt{\lambda+w}(\lambda+w\cos\chi)}\left[1-\frac{(\lambda+\delta)^2(\gamma+1)M_\infty^4}{2\beta_\infty^4 w^2}\right]\right)d\lambda\\ &-\frac{(\gamma+1)M_\infty^4}{4\beta_\infty^4 w^2}\frac{\mathrm{i}\cos\theta/2}{\sqrt{R}}\int_{-\infty}^{\infty}\sqrt{\lambda-w}\frac{(\lambda+\delta)}{(\lambda+w\cos\chi)}\mathrm{e}^{a(\lambda,R,\theta)}d\lambda\\ &+\mathrm{sgn}(\Psi)\frac{(\gamma+1)M_\infty^4}{4\beta_\infty^4 w^2}\frac{\sin\theta/2}{\sqrt{R}}\int_{-\infty}^{\infty}\frac{\lambda(\lambda+\delta)}{\sqrt{\lambda+w}(\lambda+w\cos\chi)}\mathrm{e}^{a(\lambda,R,\theta)}d\lambda\Big). \qquad (2.8.0.1)\end{aligned}$$

This particular solution has singular behaviour at the origin which we can analyse by defining

$$I_2(R,\theta)=\int_{-\infty}^{\infty}\sqrt{\lambda-w}\left(\frac{1}{(\lambda+w\cos\chi)}-\frac{(\gamma+1)M_\infty^4}{2\beta_\infty^4 w^2}\frac{(\lambda+\delta)^2}{(\lambda+w\cos\chi)}\right)\mathrm{e}^{a(\lambda,R,\theta)}d\lambda, \qquad (2.8.0.2)$$

$$I_3(R,\theta)=\int_{-\infty}^{\infty}\frac{\lambda}{\sqrt{\lambda+w}}\left(\frac{1}{(\lambda+w\cos\chi)}-\frac{(\gamma+1)M_\infty^4}{2\beta_\infty^4 w^2}\frac{(\lambda+\delta)^2}{(\lambda+w\cos\chi)}\right)\mathrm{e}^{a(\lambda,R,\theta)}d\lambda, \qquad (2.8.0.3)$$

$$I_4(R,\theta)=\int_{-\infty}^{\infty}\sqrt{\lambda-w}\frac{(\lambda+\delta)}{(\lambda+w\cos\chi)}\mathrm{e}^{a(\lambda,R,\theta)}d\lambda, \qquad (2.8.0.4)$$

$$I_5(R,\theta)=\int_{-\infty}^{\infty}\frac{\lambda}{\sqrt{\lambda+w}}\frac{(\lambda+\delta)}{(\lambda+w\cos\chi)}\mathrm{e}^{a(\lambda,R,\theta)}d\lambda. \qquad (2.8.0.5)$$

These represent the integrals in (2.8.0.1). There is a clear similarity to the gust case considered by Tsai (1992), so we evaluate these integrals as he does; we can write

[1] This method is repeated in detail in the first appendix of the next chapter. We have chosen to include full details of the method for that solution because of the errors found in Tsai (1992).

$$I_2(R,\theta) = -2\pi\sqrt{1+\cos\chi}V(\chi)\mathrm{e}^{\mathrm{i}wR(\cos\chi\,\cos\theta-|\sin\theta||\sin\chi|)} + 2\mathrm{e}^{\mathrm{i}wR\cos\theta+\pi\mathrm{i}/4}\left(I_{21}(R,\theta)+\frac{(\gamma+1)M_\infty^4}{2\beta_\infty^4 w^2}I_{22}(R,\theta)\right), \tag{2.8.0.6}$$

$$I_3(R,\theta) = \frac{2\pi\mathrm{i}\sqrt{w}\cos\chi}{\sqrt{1-\cos\chi}}V(\chi)\mathrm{e}^{\mathrm{i}wR(\cos\chi\,\cos\theta-|\sin\theta||\sin\chi|)} + 2\mathrm{e}^{\mathrm{i}wR\cos\theta-\pi\mathrm{i}/4}\left(I_{31}(R,\theta)+\frac{(\gamma+1)M_\infty^4}{2\beta_\infty^4 w^2}I_{32}(R,\theta)\right), \tag{2.8.0.7}$$

$$I_4(R,\theta) = -2\pi\sqrt{1+\cos\chi}(\delta-w\cos\chi)\mathrm{e}^{\mathrm{i}wR(\cos\chi\,\cos\theta-|\sin\theta||\sin\chi|)} + 2\mathrm{e}^{\mathrm{i}wR\cos\theta-\pi\mathrm{i}/4}I_{41}(R,\theta), \tag{2.8.0.8}$$

$$I_5(R,\theta) = -\frac{2\pi\mathrm{i}\sqrt{w}\cos\chi}{\sqrt{1-\cos\chi}}(\delta-w\cos\chi)\mathrm{e}^{\mathrm{i}wR(\cos\chi\,\cos\theta-|\sin\theta||\sin\chi|)} + 2\mathrm{e}^{\mathrm{i}wR\cos\theta+\pi\mathrm{i}/4}I_{51}(R,\theta), \tag{2.8.0.9}$$

and evaluate in the limit $R\to 0$ to get

$$I_{22}\sim\sqrt{\pi}\left(\frac{3}{4R^{5/2}}\sin\frac{3\theta}{2}+\frac{\mathrm{i}}{8R^{3/2}}\left[(8\delta-4w\cos\chi-5w)\sin\frac{3\theta}{2}-3w\sin\frac{7\theta}{2}\right]\right), \tag{2.8.0.10}$$

$$I_{32}\sim\sqrt{\pi}\left(\frac{3}{4R^{5/2}}\cos\frac{3\theta}{2}+\frac{\mathrm{i}}{8R^{3/2}}\left[(8\delta-4w\cos\chi-5w)\cos\frac{3\theta}{2}-3w\cos\frac{7\theta}{2}\right]\right), \tag{2.8.0.11}$$

$$I_{41}\sim\sqrt{\pi}\left(\frac{1}{2R^{3/2}}\sin\frac{3\theta}{2}+\frac{\mathrm{i}}{4\sqrt{R}}\left[-2w\cos\frac{3\theta}{2}\sin\theta+4(\delta-w\cos\chi-w)\sin\frac{\theta}{2}\right]\right), \tag{2.8.0.12}$$

$$I_{51}\sim\sqrt{\pi}\left(\frac{1}{2R^{3/2}}\cos\frac{3\theta}{2}+\frac{\mathrm{i}}{4\sqrt{R}}\left[2w\sin\frac{3\theta}{2}\sin\theta+4(\delta-w\cos\chi-w)\cos\frac{\theta}{2}\right]\right). \tag{2.8.0.13}$$

We have neglected terms that do not create singularities at $R=0$. By summing and simplifying we find that the asymptotic behaviour of this solution as $R\to 0$ is

$$\hat{H}_{3p}\sim\frac{\mathrm{i}\sin\chi\, a\mathrm{e}^{\mathrm{i}\pi/4}(\gamma+1)M_\infty^4}{2\sqrt{\pi}\beta_\infty^3 w\sqrt{w\cos\chi+w}}\left(\frac{\sin 2\theta}{R^2}+\frac{\mathrm{i}\delta\sin\theta}{R}\right). \tag{2.8.0.14}$$

We can approximate the terms in (2.2.4.1a) for small R, and then integrate the resulting equation to give us a local solution of (2.2.4.1a) valid for small R. This informs us that H_3 ought not be singular at $R=0$. Hence we add the appropriate Hankel functions, which are complementary solutions to the Helmholtz equation, to eliminate the singularity to yield

$$H_{3p} = \hat{H}_{3p} + \frac{a \sin\chi \, \mathrm{e}^{\mathrm{i}\pi/4}(\gamma+1)M_\infty^4\sqrt{\pi}}{4\beta_\infty^3 w^{3/2}\sqrt{\cos\chi+1}}\left(\frac{w}{2}\mathrm{H}_2^{(1)}(wR)\sin 2\theta + \mathrm{i}\delta \mathrm{H}_1^{(1)}(wR)\sin\theta\right), \tag{2.8.0.15}$$

where $H_{1,2}^{(1)}$ are Hankel functions of the first kind (Abramowitz and Stegun 1964, p. 358). We define $H_{3p}^* = H_{3p} - \hat{H}_{3p}$.

2.9 Leading-Edge Inner Solutions H_{3c_i}

Equation (2.2.4.3c) is factored as $d_1 + d_2 + d_3$, where

$$d_1(\Phi) = -\frac{\beta_\infty a}{w}\mathrm{e}^{\mathrm{i}w\cos\chi\,\Phi}\left(-2w^2\sin^2\chi\sqrt{\Phi} - \frac{\mathrm{i}w\cos\chi}{\sqrt{\Phi}} - \frac{\mathrm{i}(\gamma+1)M_\infty^4}{2\beta_\infty^4 w^2}\frac{(\delta - w\cos\chi)}{2}\left[-4\sqrt{\Phi}(\delta - w\cos\chi)w^2\sin^2\chi + \frac{2\mathrm{i}(w\cos\chi(\delta - 2w\cos\chi)+w^2)}{\sqrt{\Phi}}\right]\right), \tag{2.9.0.1}$$

$$d_2(\Phi) = \frac{\mathrm{i}w\sin\chi\,\beta_\infty a\,\mathrm{e}^{\mathrm{i}w\Phi+\mathrm{i}\pi/4}}{\sqrt{\pi}\sqrt{w\cos\chi+w}}\frac{1}{\cos\chi-1}\left(1 - \frac{(\gamma+1)M_\infty^4}{2\beta_\infty^4 w^2}(\delta-w)^2\right)\frac{1}{\Phi}, \tag{2.9.0.2}$$

$$\begin{aligned} d_3(\Phi) = {} & \frac{\mathrm{i}w\sin\chi\,\beta_\infty a\,\mathrm{e}^{\mathrm{i}w\Phi+\mathrm{i}\pi/4}}{\sqrt{\pi}\sqrt{w\cos\chi+w}}\left[2\mathrm{i}(w\cos\chi+w)\left(1 - \frac{(\gamma+1)M_\infty^4}{2\beta_\infty^2 w^2}(\delta-w)^2\right) - \frac{X}{\Phi}\right. \\ & + \frac{\sqrt{\pi}(\gamma+1)M_\infty^4\cos\chi}{4\beta_\infty^4 w\sqrt{w\cos\chi-w}\Phi^{3/2}}(\delta - w\cos\chi)\mathrm{e}^{\mathrm{i}(w\cos\chi-w)\Phi-\pi\mathrm{i}/4} \\ & - \frac{(\gamma+1)M_\infty^4}{2\beta_\infty^4 w^2}\left(\frac{2}{\Phi^3} + \frac{\mathrm{i}(\delta-2w)}{\Phi^2}\right) \\ & + \frac{\sqrt{\pi}\mathrm{e}^{\mathrm{i}(w\cos\chi-w)\Phi-\mathrm{i}\pi/4}}{\sqrt{w\cos\chi-w}}\mathrm{erfc}(\mathrm{e}^{\mathrm{i}\pi/4}\sqrt{(w\cos\chi-w)\Phi})\left[-2w^2\sin^2\chi\sqrt{\Phi}\right. \\ & - \frac{\mathrm{i}w\cos\chi}{\sqrt{\Phi}} - \frac{\mathrm{i}(\gamma+1)M_\infty^4}{4\beta_\infty^4 w^2}(\delta - w\cos\chi)\left(-4\sqrt{\Phi}(\delta-w\cos\chi)w^2\sin^2\chi\right. \\ & \left.\left.\left. + \frac{2i((\delta-2w\cos\chi)w\cos\chi+w^2)}{\sqrt{\Phi}} + \frac{w\cos\chi}{\Phi^{3/2}}\right)\right]\right] \\ & + \frac{aM_\infty^2\mathrm{e}^{\mathrm{i}w\cos\chi\Phi}}{2\beta_\infty\Phi^{3/2}}\mathrm{erf}(\mathrm{e}^{\mathrm{i}\pi/4}\sqrt{(w\cos\chi-w)\Phi}) \\ & - \frac{(\gamma+1)M_\infty^4\sin\chi\,a\sqrt{\pi}}{4\beta_\infty^3\sqrt{w\cos\chi+w}}\mathrm{e}^{\pi\mathrm{i}/4}\left(wH_2^{(1)}(w\Phi) + \mathrm{i}\delta H_1^{(1)}(w\Phi)\right)\frac{1}{\Phi}, \end{aligned} \tag{2.9.0.3}$$

and

$$X = \frac{1}{\cos\chi - 1}\left(1 + \frac{(\gamma+1)M_\infty^4}{2\beta_\infty^4 w^2}\left[w(\cos\chi - 1)^2(w\cos\chi + w - \delta) + (\delta - w)^2\right]\right). \tag{2.9.0.4}$$

We assume that δ has a small positive imaginary part so that when we apply the Fourier transform, our integrals converge at infinity. The F_{+i} required for the evaluation of the L_{3c_i} in Sect. 2.2.4 are given by

$$F_{+i} = \int_0^\infty \frac{d_i(x)\mathrm{e}^{\mathrm{i}\lambda x}}{\sqrt{\lambda - w}}\mathrm{erf}(\mathrm{e}^{\mathrm{i}\pi/4}\sqrt{(\lambda - w)x})dx. \tag{2.9.0.5}$$

We evaluate $F_{+1,2}$, noting that the formula

$$F_{+i}(\lambda) = \frac{1}{2\pi\mathrm{i}}\int_{C_1}\frac{d\kappa}{\sqrt{\kappa - w}(\kappa - \lambda)}\int_0^\infty d_i(x)\mathrm{e}^{\mathrm{i}\kappa x}dx \tag{2.9.0.6}$$

(where the contour of integration, C_1, runs parallel to, but just above, the real κ axis, and below w), is more appropriate to evaluate $F_{+1,2}$ since it allows us to properly assess the effects of the branch cuts. For F_{+1} we evaluate the x integral in (2.9.0.6) first, whereas for F_{2+} is it easier to evaluate the κ integral first. We obtain

$$\begin{aligned} F_{+1} =& \frac{-\mathrm{i}\beta_\infty a\mathrm{e}^{3\mathrm{i}\pi/4}}{\sqrt{\pi}}\left(\frac{-\mathrm{i}(\alpha - wb\cos\chi)}{(w + w\cos\chi)(\lambda + w\cos\chi)}\right. \\ &\left. - \frac{\pi}{2}\frac{\alpha + \lambda b}{\sqrt{\lambda - w}(w\cos(\chi) + \lambda)^{3/2}}\left[1 - \frac{2}{\pi}\arcsin\left(\frac{\sqrt{w - \lambda}}{\sqrt{w + w\cos\chi}}\right)\right]\right), \end{aligned} \tag{2.9.0.7}$$

where

$$\begin{aligned} \alpha &= -2w^2 + \frac{\mathrm{i}M_\infty^4(\gamma+1)}{\beta_\infty^2}(\delta - w\cos\chi)^2, \\ b &= -2w\cos\chi - \frac{\mathrm{i}M_\infty^4(\gamma+1)}{\beta_\infty^2 w}(\delta - w\cos\chi)\left(\cos\chi(\delta - 2w\cos\chi) + w\right), \end{aligned}$$

and

$$\begin{aligned} F_{+2} =& \frac{2\mathrm{i}\sin\chi\sqrt{w}\beta_\infty a\mathrm{e}^{\mathrm{i}\pi/4}}{\sqrt{\pi}\sqrt{\cos\chi + 1}\sqrt{\lambda - w}}\frac{1}{\cos\chi - 1}\left(1 - \frac{(\gamma+1)M_\infty^4}{2\beta_\infty^4 w^2}(\delta - w)^2\right) \\ &\times \log\left[\frac{\sqrt{2w} - \mathrm{i}\sqrt{\lambda - w}}{\sqrt{\lambda + w}}\right]. \end{aligned} \tag{2.9.0.8}$$

The decomposition of the complementary solution is done in this way so that we may explicitly evaluate L_{3c_1} and L_{3c_2}. The remaining terms for the integral involved in L_{3c_3} is convergent, but must be evaluated numerically. We take the outer limits of the H_{3c_i} given by (2.2.4.4b) to find the directivity functions L_{3c_i}. We find

$$L_{3c_1}(\theta) = -\frac{\beta_\infty a \,\mathrm{sgn}(\Psi)\cos(\theta/2)}{2\sqrt{2}w(\cos\chi-\cos\theta)}\left[\frac{\alpha - wb\cos\theta}{w\sqrt{\cos\chi-\cos\theta}}\left(1-\frac{2}{\pi}\arcsin\left[\frac{\sqrt{1+\cos\theta}}{\sqrt{1+\cos\chi}}\right]\right)\right.$$
$$\left. -\frac{2}{\pi}\frac{(\alpha - w\cos(\chi)b)\sqrt{1+\cos\theta}}{w\cos\chi + w}\right], \tag{2.9.0.9}$$

This is not singular at $\cos\theta = \cos\chi$ which can be seen by taking a Taylor series expansion for θ close to χ. In Ayton and Peake (2013) we incorrectly thought L_{3c_1} was singular at $\cos\theta = \cos\chi$ and presented a complementary error function style uniformly-valid solution, which given the parameter β, (2.2.1.7b), would never be $O(1)$ (as we have now established that there is no singularity) is equivalent to the result presented here.

The uniformly-valid expansion of L_{3c_2} found by using Van der Waerden's method (Van der Waerden 1952)[2] is

$$L^u_{3c_2}(r,\theta) = \frac{\sqrt{2}\mathrm{sgn}(\Psi)\sin\chi\,\beta_\infty a}{\pi\sqrt{\cos\chi+1}}\frac{1}{\cos\chi-1}\left(1-\frac{(\gamma+1)M_\infty^4}{2\beta_\infty^4 w^2}(\delta-w)^2\right)$$
$$\left[\frac{\sqrt{2}}{\sqrt{\pi}\sqrt{1+\cos\theta}}\left(\frac{\sqrt{\pi}}{2}\log(kr) - \int_{-\infty}^{\infty}\log(s+\mathrm{e}^{\mathrm{i}\pi/4}\sqrt{w(1-\cos\theta)kr})\mathrm{e}^{-s^2}ds\right)\right.$$
$$\left. + \log\left(\frac{\sqrt{2}+\sqrt{1+\cos\theta}}{\sqrt{1-\cos\theta}}\right) + \frac{\log(1-\cos\theta)}{\sqrt{2}\sqrt{1+\cos\theta}} + \frac{i\pi + 2\log(w)}{2\sqrt{2}\sqrt{1+\cos\theta}}\right], \tag{2.9.0.10}$$

so that

$$H^u_{3c_2} \sim L^u_{3c_2}(r,\theta)\frac{\mathrm{e}^{\mathrm{i}kwr}}{\sqrt{kr}}. \tag{2.9.0.11}$$

The logarithmic singularity at $\theta = 0$ has now been removed, as the singular contributions of the second and third to last terms in (2.9.0.10) cancel. This singularity occurs originally at $\theta = O(k^{-1/2})$ in the integral expression of the H_{3c_2} Wiener-Hopf solution (see (2.9.0.8)) , which we shall see later is a key scaling for the leading-edge transition solution. Finally

[2] Again, full details of this method will be covered in the first appendix of the next chapter because of errors in Tsai's results.

$$L_{3c_3}(\theta) = -\frac{\operatorname{sgn}(\psi)\mathrm{e}^{\mathrm{i}\pi/4}}{\sqrt{2\pi w}} \int_0^\infty \mathrm{e}^{-\mathrm{i}w\cos\theta x} \operatorname{erf}(\mathrm{e}^{-\mathrm{i}\pi/4}\sqrt{w(1+\cos\theta)x}) d_3(x)dx \tag{2.9.0.12}$$

is retained in integral form as it is not possible to find an analytic expression for this integral; it must be evaluated numerically.

2.10 Pressure Jump Across the Trailing Edge

The thickness-related total leading-edge solution for $\phi > 2$ on $\psi = 0_\pm$ is given by $h_l^{(t)}(\phi, 0_\pm) + h_{ls}^{(t)}(\phi, 0_\pm)$, using the expression for G as given in (2.3.2.5b), so

$$\begin{aligned} h_l^{u(t)}(\phi, 0_\pm) = \frac{\mathrm{e}^{\mathrm{i}kw\sigma_l(\phi,0)}}{\sqrt{k\phi}} \Bigg(& L_0(0_\pm) + t\sqrt{k}\Big[L_1(0_\pm) + L_2(0_\pm) + L_{3p}(0_\pm) + L_{3c_1}(0_\pm) \\ & + L_{3c_3}(0_\pm) \mp \frac{\beta_\infty \sin\chi}{\sqrt{2\pi}\sqrt{\cos\chi+1}(\cos\chi-1)} \left(1 - \frac{(\gamma+1)M_\infty^4}{2\beta_\infty^4 w^2}(\delta-w)^2\right) \Bigg\{ \int_0^2 \Bigg[\frac{a}{\xi} \\ & + \frac{\beta_\infty}{t'\xi^{3/2}} \int_0^\xi \frac{\partial q^{(t)}}{\partial\theta}(r',0)dr' \Bigg] \frac{\sqrt{\phi}}{\sqrt{\phi-\xi}} d\xi + \int_2^\phi \Bigg[\frac{a}{\xi} + \frac{\beta_\infty}{t'\xi^{3/2}} \int_0^2 \frac{\partial q^{(t)}}{\partial\theta}(r',0)dr' \Bigg] \frac{\sqrt{\phi}}{\sqrt{\phi-\xi}} d\xi \\ & - \frac{a}{2}\left(\log[32k\phi w] + \tilde{\gamma} - \frac{\pi\mathrm{i}}{2}\right) \Bigg\} \Big] \Bigg). \end{aligned} \tag{2.10.0.1}$$

The final term in this expression occurs due to the contribution from the non-uniformity in L_{3c_2} at $\theta = 0_\pm$ and can be seen by setting $\theta = 0$ in (2.9.0.10), using Gradshteyn and Ryzhik (1980, p. 574). Equation (2.10.0.1) forms the basis of the pressure jump across the trailing edge, which is given by

$$\begin{aligned} p_l|_{\psi=0+} - p_l|_{\psi=0-} = & \frac{\mathrm{i}(\delta-w)}{\sqrt{k}\sqrt{2+\phi_t}} \mathrm{e}^{\mathrm{i}k(w-\delta M_\infty^2)(2+\phi_t+\alpha_t)+\mathrm{i}kw\epsilon V(0)\int_0^\phi q(r',0)dr'+\mathrm{i}kw\epsilon\sigma_1(0,0)} \\ & \Big[\mathrm{e}^{\mathrm{i}k(w-\delta M_\infty^2)\Gamma/2} \Big\{ P_l(0) + t\sqrt{k}[L_1(0) + L_2(0) + L_{3p}(0) + L_{3c_1}(0) + L_{3c_2}(0) + L_{3c_3}(0)] \\ & - t\sqrt{k}\frac{\sin\chi\,\beta_\infty}{\sqrt{2\pi}\sqrt{\cos\chi+1}(\cos\chi-1)} \left(1 - \frac{(\gamma+1)M_\infty^4}{2\beta_\infty^4 w^2}(\delta-w)^2\right) \Big\{ \int_0^2 \Big[\frac{a}{\xi} \\ & + \frac{\beta_\infty}{t'\xi^{3/2}} \int_0^\xi \frac{\partial q^{(t)}}{\partial\theta}(r',0)dr' \Big] \frac{\sqrt{2+\phi_t}}{\sqrt{2+\phi_t-\xi}} d\xi + \int_2^{2+\phi_t} \Big[\frac{a}{\xi} + \frac{\beta_\infty}{t'\xi^{3/2}} \int_0^2 \frac{\partial q^{(t)}}{\partial\theta}(r',0)dr' \Big] \\ & \frac{\sqrt{2+\phi_t}}{\sqrt{2+\phi_t-\xi}} d\xi - \frac{a}{2}\left(\log[32k(\phi_t+2)w] + \tilde{\gamma} - \frac{\pi\mathrm{i}}{2}\right) \Big\} \Big] \Big\} - \Big[\mathrm{e}^{-\mathrm{i}k(w-\delta M_\infty^2)\Gamma/2} \Big\{ P_l(2\pi) \\ & + t\sqrt{k}[L_1(2\pi) + L_2(2\pi) + L_{3p}(2\pi) + L_{3c_1}(2\pi) + L_{3c_2}(2\pi) + L_{3c_3}(2\pi)] \\ & + t\sqrt{k}\frac{\sin\chi\,\beta_\infty}{\sqrt{2\pi}\sqrt{\cos\chi+1}(\cos\chi-1)} \left(1 - \frac{(\gamma+1)M_\infty^4}{2\beta_\infty^4 w^2}(\delta-w)^2\right) \\ & \Big\{ \int_0^2 \Big[\frac{a}{\xi} + \frac{\beta_\infty}{t'\xi^{3/2}} \int_0^\xi \frac{\partial q^{(t)}}{\partial\theta}(r',0)dr' \Big] \frac{\sqrt{2+\phi_t}}{\sqrt{2+\phi_t-\xi}} d\xi \end{aligned}$$

$$+\int_2^{2+\phi_t}\left[\frac{a}{\xi}+\frac{\beta_\infty}{t'\xi^{3/2}}\int_0^2\frac{\partial q^{(t)}}{\partial\theta}(r',0)dr'\right]\frac{\sqrt{2+\phi_t}}{\sqrt{2+\phi_t-\xi}}d\xi$$
$$-\frac{a}{2}\left(\log[32k(\phi_t+2)w]+\tilde{\gamma}-\frac{\pi\mathrm{i}}{2}\right)\Bigg]\Bigg\}+\epsilon\sqrt{k}\frac{\mathrm{e}^{\pi\mathrm{i}/4}iV(0)}{\sqrt{\pi w}\beta_\infty}\int_0^2\frac{\xi y^{(c)\prime}(\xi)-y^{(c)}(\xi)}{\sqrt{2-\xi}\xi^{3/2}}d\xi$$
$$\left(\mathrm{e}^{\mathrm{i}k(w-\delta M_\infty^2)\Gamma/2}P_l(0)+\mathrm{e}^{-\mathrm{i}k(w-\delta M_\infty^2)\Gamma/2}P_l(2\pi)\right)\Bigg]. \qquad (2.10.0.2)$$

We write the pressure jump in the form (2.4.2.2) where

$$\Delta p^{(t)}(\phi_t)=\frac{\sqrt{2}}{\sqrt{2+\phi_t}}\Delta p^{(t)}(0)+t\sqrt{k}\frac{\mathrm{i}w\sin\chi\,\beta_\infty\sqrt{w}}{\sqrt{2}\pi\sqrt{\delta+w}}\mathrm{e}^{\mathrm{i}k(w-\delta M_\infty^2)(2+\alpha_t)+\mathrm{i}kw\epsilon\sigma_1'(0,0)}$$
$$\left(1-\frac{(\gamma+1)M_\infty^4}{2\beta_\infty^4w^2}(\delta-w)^2\right)\Bigg\{\mathrm{e}^{\mathrm{i}k(w-\delta M_\infty^2)\Gamma/2}\mathrm{e}^{\mathrm{i}kw\epsilon\sigma_{l1}(2,0)}\left(\int_0^2\left[\frac{a}{\xi}\right.\right.$$
$$\left.+\frac{\beta_\infty}{t'\xi^{3/2}}\int_0^\xi\frac{\partial q^{(t)}}{\partial\theta}(r',0)dr'\right]\left(\frac{1}{\sqrt{2+\phi_t-\xi}}-\frac{\sqrt{2}}{\sqrt{2-\xi}\sqrt{2+\phi_t}}\right)d\xi$$
$$-\frac{a}{\sqrt{2}\sqrt{2+\phi_t}}\log\left[\frac{\phi_t+2}{2}\right]+\int_2^{2+\phi_t}\left[\frac{a}{\xi}+\frac{\beta_\infty}{t'\xi^{3/2}}\int_0^2\frac{\partial q^{(t)}}{\partial\theta}(r',0)dr'\right]\frac{1}{\sqrt{2+\phi_t-\xi}}d\xi\Bigg)$$
$$+\mathrm{e}^{-\mathrm{i}k(w-\delta M_\infty^2)\Gamma/2}\mathrm{e}^{\mathrm{i}kw\epsilon\sigma_{l1}(2,2\pi)}\left(\int_0^2\left[\frac{a}{\xi}\right.\right.+\frac{\beta_\infty}{t'\xi^{3/2}}\int_0^\xi\frac{\partial q^{(t)}}{\partial\theta}(r',2\pi)dr'\Bigg]$$
$$\left(\frac{1}{\sqrt{2+\phi_t-\xi}}-\frac{\sqrt{2}}{\sqrt{2-\xi}\sqrt{2+\phi_t}}\right)d\xi-\frac{a}{\sqrt{2}\sqrt{2+\phi_t}}\log\left[\frac{\phi_t+2}{2}\right]$$
$$\left.+\int_2^{2+\phi_t}\left[\frac{a}{\xi}+\frac{\beta_\infty}{t'\xi^{3/2}}\int_0^2\frac{\partial q^{(t)}}{\partial\theta}(r',2\pi)dr'\right]\frac{1}{\sqrt{2+\phi_t-\xi}}d\xi\right)\Bigg\}. \qquad (2.10.0.3)$$

References

Abbott, I. H., & Von Doenhoff, A. E. (1959). *Theory of wing sections, including a summary of airfoil data*. New York: Courier Dover Publications.

Abramowitz, M., & stegun, I. A. (1964). *Handbook of mathematical functions: With formulas, graphs, and mathematical tables*. New York: Courier Dover Publications.

Ayton, L. J., & Peake, N. (2013). On high-frequency noise scattering by aerofoils in flow. *Journal of Fluid Mechanics*, *734*, 144–182.

Bleistein, N., & Handelsman, R. A. (1975). *Asymptotic expansions of integrals*. New York: Ardent Media.

Crighton, D. G. (1985). The Kutta condition in unsteady flow. *Annual Review of Fluid Mechanics*, *17*, 411–445.

Ffowcs Williams, J. E., & Hawkings, D. L. (1969). Sound generation by turbulence and surfaces in arbitrary motion. *Philosophical Transactions of the Royal Society A*, *264*, 321–342.

Goldstein, M. E. (1978). Unsteady vortical and entropic distortions of potential flows round arbitrary obstacles. *Journal of Fluid Mechanics*, *89*, 433–468.

Gradshteyn, I. S., & Ryzhik, I. M. (1980). *Table of integrals, series, and products* (6th ed.). New York: Academic Press.

Howe, M. S. (1978). *A review of the theory of trailing edge noise. Contractor Report Jul Dec 1977* (Vol. 61, pp. 437–465). Cambridge MA: Bolt Beranek and Newman Inc.

Hunt, J. C. R. (1973). A theory of turbulent flow round two-dimensional bluff bodies. *Journal of Fluid Mechanics*, *61*, 625–706.

Jones, D. S. (1966). *Generalised functions*. New York: McGraw-Hill.

Jones, D. S. (1986). *Acoustic and electromagnetic waves*. Oxford: Clarendon Press.

Kerschen, E. J., & Balsa, T. F. (1981). Transformation of the equation governing disturbances of a two-dimensional compressible flow. *AIAA Journal*, *19*, 1367–1370.

Kerschen, E. J., & Myers, M. R. (1987). Perfect gas effects in compressible rapid distortion theory. *AIAA Journal*, *25*, 504–507.

Myers, M. R. (1987). Effect of airfoil mean loading on high-frequency gust interaction noise (PhD thesis, University of Arizona).

Myers, M. R., & Kerschen, E. J. (1995). Influence of incidence angle on sound generation by airfoils interacting with high-frequency gusts. *Journal of Fluid Mechanics*, *292*, 271–304.

Myers, M. R., & Kerschen, E. J. (1997). Influence of camber on sound generation by airfoils interacting with high-frequency gusts. *Journal of Fluid Mechanics*, *353*, 221–259.

Noble, B. (1998). *Methods based on the Wiener-Hopf technique for the solution of partial differential equations*. New York: Chelsea Publications.

Peake, N., & Kerschen, E. J. (2004). Influence of mean loading on noise generated by the interaction of gusts with a cascade: Downstream radiation. *Journal of Fluid Mechanics*, *515*, 99–133.

Thwaites, B. (1960). *Incompressible aerodynamics: An account of the theory and observation of the steady flow of incompressible fluid past aerofoils, wings, and other bodies*. New York: Dover Publications.

Tsai, C. -T. (1992). Effect of airfoil thickness on high-frequency gust interaction noise (PhD thesis, University of Arizona).

Van der Waerden, B. L. (1952). On the method of saddle points. *Applied Scientific Research, Section B*, *2*, 33–45.

Van Dyke, M. (1975). *Perturbation methods in fluid mechanics*. Stanford: Parabolic Press.

http://www.springer.com/978-3-319-19958-0

Asymptotic Approximations for the Sound Generated by Aerofoils in Unsteady Subsonic Flows

Ayton, L.

2015, XXI, 178 p. 48 illus., 6 illus. in color., Hardcover
ISBN: 978-3-319-19958-0